iScience

CellPress
OPEN ACCESS

Article

Densities and numbers of calbindin and parvalbumin positive neurons across the rat and mouse brain

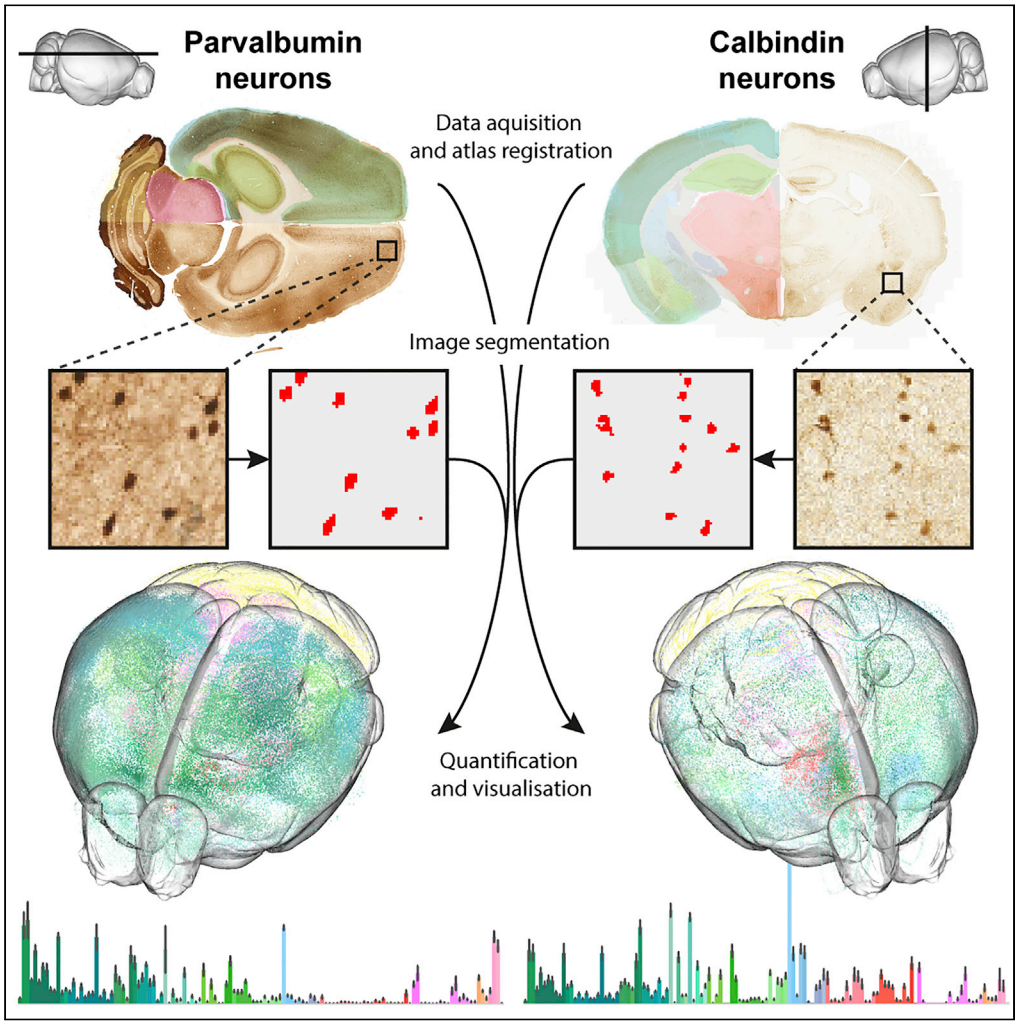

Ingvild E. Bjerke, Sharon C. Yates, Arthur Laja, Menno P. Witter, Maja A. Puchades, Jan G. Bjaalie, Trygve B. Leergaard

t.b.leergaard@medisin.uio.no

Highlights

Brain-wide, semi-automatic quantification of parvalbumin and calbindin neurons

Largely complementary distribution of calbindin and parvalbumin neurons in mice

Comparison with several previous studies shows variable numbers but similar trends

Similar distribution of parvalbumin neurons in the rat and mouse hippocampal region

Bjerke et al., iScience *24*, 101906
January 22, 2021
https://doi.org/10.1016/j.isci.2020.101906

iScience

CellPress
OPEN ACCESS

Article

Densities and numbers of calbindin and parvalbumin positive neurons across the rat and mouse brain

Ingvild E. Bjerke,[1] Sharon C. Yates,[1] Arthur Laja,[2] Menno P. Witter,[2] Maja A. Puchades,[1] Jan G. Bjaalie,[1] and Trygve B. Leergaard[1,3,*]

Summary

The calcium-binding proteins parvalbumin and calbindin are expressed in neuronal populations regulating brain networks involved in spatial navigation, memory processes, and social interactions. Information about the numbers of these neurons across brain regions is required to understand their functional roles but is scarcely available. Employing semi-automated image analysis, we performed brain-wide analysis of immunohistochemically stained parvalbumin and calbindin sections and show that these neurons distribute in complementary patterns across the mouse brain. Parvalbumin neurons dominate in areas related to sensorimotor processing and navigation, whereas calbindin neurons prevail in regions reflecting behavioral states. We also find that parvalbumin neurons distribute according to similar principles in the hippocampal region of the rat and mouse brain. We validated our results against manual counts and evaluated variability of results among researchers. Comparison of our results to previous reports showed that neuron numbers vary, whereas patterns of relative densities and numbers are consistent.

Introduction

Transient increases in intracellular calcium concentrations play a critical role in the regulation of neuronal excitability, neurotransmitter release, and synaptic plasticity (Berridge, 1998). The spatial and temporal dynamics of such calcium signals can be modulated by calcium-binding proteins, which are widely expressed in the nervous system (Schwaller, 2010). Two such proteins, parvalbumin and calbindin, are expressed in largely non-overlapping groups of neurons that show fast-spiking and bursting electrophysiological phenotypes, respectively (Markram et al., 2004).

Parvalbumin is expressed in a group of interneurons characterized by fast responses and effective inhibition of surrounding principal neurons (Hu et al., 2014). The role of parvalbumin neurons in fine-tuning networks of principal neurons has been widely investigated in deep layers of somatosensory and visual cortices (Atallah et al., 2012; Runyan et al., 2010; Yu et al., 2016, 2019a). In association with cortices, parvalbumin neurons are less prominent in deeper layers, and interestingly, in parahippocampal domains they are primarily seen in superficial layers (Boccara et al., 2015). A well-studied example is the parvalbumin neuron in the medial entorhinal cortex, known for its characteristic grid cells, which have multiple firing fields making up a triangular array across the entire environment available to an animal (Hafting et al., 2005). Parvalbumin interneurons are key modulators of these cells, particularly in layer II networks, where principal neurons communicate through parvalbumin interneurons (Couey et al., 2013; Miao et al., 2017). Similar principles of inhibitory connectivity has been shown in the lateral entorhinal cortex (Nilssen et al., 2018), where principal cells are tuned to the past and present positions of objects (Tsao et al., 2013) and groups of cells are involved in representing sequences of event (Tsao et al., 2018). Beyond the role of parvalbumin neurons in parahippocampal circuits, the importance of these interneurons across the brain is supported by their dysfunction in several neuropsychiatric and developmental disorders (Ferguson and Gao, 2018; for review, see Marín, 2012), including autism spectrum disorders (Gogolla et al., 2009), Tourette syndrome (Kalanithi et al., 2005) and schizophrenia (Gonzalez-Burgos and Lewis, 2012; Hashimoto et al., 2003).

[1]Department of Molecular Medicine, Institute of Basic Medical Sciences, University of Oslo, Oslo, Norway

[2]Kavli Institute for Systems Neuroscience, Norwegian University of Science and Technology, Trondheim, Norway

[3]Lead Contact

*Correspondence: t.b.leergaard@medisin.uio.no

https://doi.org/10.1016/j.isci.2020.101906

Calbindin-D28k is expressed in populations of excitatory and inhibitory neurons (Jinno and Kosaka, 2006; Szabadics et al., 2010). Other calbindin proteins include calbindin-D9k, primarily expressed in epithelial cells, and calretinin, which is expressed in neuronal cells and to a degree co-localizes with calbindin-D28k (Lu et al., 2009; Rogers and Résibois, 1992). In this study, we focus on neurons expressing calbindin-D28k, in the following referred to as calbindin neurons. In the neocortex, calbindin is typically associated with interneurons (Ascoli et al., 2008; Markram et al., 2004), but this protein is also found to be expressed in pyramidal neurons, e.g. in the medial entorhinal cortex (Ray et al., 2014) and CA1 (Merino-Serrais et al., 2020). Calbindin-positive neurons thus probably represent both interneurons and principal neurons, perhaps depending on the area in question, and the functional roles of calbindin neurons have been less well characterized than those of parvalbumin interneurons. However, recent evidence shows that selective knockdown of calbindin neurons in the CA1 and dentate gyrus regions of the hippocampus can reduce long-term potentiation, pointing to a role for these neurons in memory function (Li et al., 2017). Calbindin neurons have also been implicated in fear memory and social behavior (Harris et al., 2016) and have been hypothesized to have a neuroprotective role (Sun et al., 2011).

Given the well-known and proposed roles of parvalbumin and calbindin neurons in neuronal networks, quantitative information representing their number and distribution in the brain is of broad interest to neuroscientists. Such data are needed to constrain computational models, to measure group differences in intervention-based studies, and to draw conclusions about structure-function relationships. Several studies have quantified neurons expressing calcium-binding proteins in one or a few brain regions (see, e.g. Andsberg et al., 2001; Pitts et al., 2013; Schmid et al., 2013; Yalcin-Cakmakli et al., 2018). Studies on a larger scale have typically been qualitative or semi-quantitative (Arai et al., 1994; Frantz and Tobin, 1994), whereas one study has reported brain-wide quantitative data about parvalbumin neurons in Cre reporter mice (Kim et al., 2017). Others have focused on gathering measurements from the literature and calculating values for parameters that have yet to be tested experimentally (Bezaire and Soltesz, 2013). However, there is growing awareness that numbers reported in the literature are prone to substantial variability across publications (Bjerke et al., 2020a; Keller et al., 2018). Quantitative studies of parvalbumin and calbindin neurons acquired across the brain are needed to elucidate their relative numbers and distributions within and across regions and species. Also, replication and validation of quantitative studies will be essential to converge on realistic estimates of the number of various cell types.

Computational methods for automated segmentation, localization, and quantification of cells have successfully been applied to three-dimensional volumetric datasets to generate region- or brain-wide estimates of cell numbers in mice (Kim et al., 2017; Murakami et al., 2018; Silvestri et al., 2015; Zhang et al., 2017). These efforts have relied on advanced volumetric imaging techniques, genetically modified animals expressing fluorescent signals in cells of interest, and custom codes for analysis. Immunohistochemical techniques continue to serve important purposes for characterizing cell populations based on protein expression (which may only be a subset of those expressing the gene for the protein). To achieve efficient quantification of immunohistochemically labeled cells in sectioned material, we used the QUINT workflow (Yates et al., 2019), which combines three open-access tools, QuickNII (Puchades et al., 2019), ilastik (Berg et al., 2019), and Nutil (Groeneboom et al., 2020). This workflow achieves quantification of segmented objects in atlas-defined regions of interest, using customized brain atlas maps, section coordinates, and machine-learning-based segmentation of the labeled objects.

We here ask how the numbers and spatial distributions of neurons expressing calcium-binding proteins vary across brain regions and possibly relate to functional or topographical patterns of organization. We quantify two largely distinct cell types identified by the calcium-binding proteins parvalbumin and calbindin in the mouse brain using the QUINT workflow and compare these with previous reports. We further quantify parvalbumin neurons in the entire rat brain and perform a detailed comparison of parvalbumin neuron numbers in the mouse and rat hippocampal regions. We validate the resulting numbers with manual counts in selected areas and assess the reliability of segmentation results between researchers. All the raw and derived datasets presented here are shared through the EBRAINS Knowledge Graph to facilitate further analysis and re-use.

Results

We used the QuickNII-ilastik-Nutil (QUINT) workflow to quantify parvalbumin neurons in the mouse and rat brain, and calbindin neurons in the mouse brain, corrected the resulting numbers with Abercrombie's

formula, and extrapolated corrected numbers to represent whole regions and volumetric densities. All data were anatomically located using the Allen Mouse Common Coordinate Framework, version 3 of the template, 2017 edition of the delineations (Wang et al., 2020; hereafter referred to as CCFv3-2017) and the Waxholm Space atlas of the Sprague-Dawley rat brain, version 1.01 of the template and version 2 of the delineations (Papp et al., 2014; Kjonigsen et al., 2015; hereafter referred to as WHSv2). Details about all procedures are provided in the Transparent methods section.

Below, we first present the quantitative data on the densities of parvalbumin and calbindin neurons in the mouse brain (n = 4 and 5, respectively), as density estimates are readily compared across regions of variable size. We go on to compare the total numbers of these cell types across the brain and analyze their relative numbers in each brain region. In addition to the text and figures presented here, all numbers and density estimates are listed in Table S1. We then compare the total number, density, and distribution of parvalbumin neurons in the mouse (n = 4) and rat (n = 4) hippocampal regions. Lastly, we compare our findings to numbers reported in the literature and assess the validity and reliability of QUINT results. All numbers reported are given as mean ± SEM; total number estimates are bilateral, whereas densities are given per mm^3. The nomenclature used here for mouse anatomical regions follows the CCFv3-2017 hierarchy (except in the cross-species comparison, where WHSv2 terms are used for both species). Some of the overarching terms from the CCFv3-2017 may not be commonly used by researchers; however, these are all listed and explained in Figure 1.

Parvalbumin neuron densities across the mouse brain

Parvalbumin neurons were most densely packed in isocortical areas and in the retrohippocampal region. Olfactory areas and areas of the hippocampal region, striatum, pallidum, and cortical subplate generally showed moderate densities, with some olfactory and amygdalar areas having high densities (Figure 2A; for details see below). Low densities were seen in the thalamus and hypothalamus, although some areas stood out with moderate amounts of parvalbumin neurons. Midbrain, pontine, and medullary regions generally showed low and moderate parvalbumin neuron densities. The density estimates for parvalbumin neurons in all gray matter regions of the mouse brain are summarized in Figure 2A, and all total number and density estimates for all mouse brain regions are included in the derived dataset.

Isocortex. Relatively high densities were seen across most isocortical areas. Auditory, visual, and somatosensory areas generally showed slightly higher densities than gustatory, visceral, and prefrontal areas. Among isocortical areas, the highest parvalbumin neuron density was seen in the anteromedial visual area (2376 ± 496), whereas the most sparse distribution was seen in the perirhinal area (666 ± 165).

Olfactory areas. The dorsal peduncular area showed the highest density of the olfactory areas (1493 ± 394), in contrast to a very low density in the accessory olfactory bulb (100 ± 48). Other olfactory areas showed a moderate density.

Hippocampal formation. The hippocampal region showed moderate densities of parvalbumin neurons. In the retrohippocampal regions, densities were generally high, with the parasubiculum showing the highest parvalbumin neuron density of all mouse brain regions (2614 ± 269). A detailed account of parvalbumin neuron densities across the hippocampal formation is given below.

Cortical subplate. Moderate parvalbumin neuron densities were seen across claustrum, entopeduncular, and amygdalar regions. The posterior amygdalar nucleus stood out among the cortical subplate regions with a relatively high density (1349 ± 499).

Cerebral nuclei. In the striatum, the dorsal (caudoputamen) part showed a higher density of parvalbumin neurons (577 ± 20) than the ventral (nucleus accumbens and fundus of striatum) region (327 ± 43). Among regions of the pallidum, the medial region showed the highest density (701 ± 238).

Thalamus and hypothalamus. The thalamic regions generally had low densities of parvalbumin neurons, except for the reticular nucleus (but this region was oversaturated with staining, and numbers are therefore not reported). The geniculate group of the ventral thalamus also showed a relatively high density (539 ± 225). The mammillary body showed the highest density among the hypothalamic regions (888 ± 172).

Figure 1. Custom regions of interest used for analysis of mouse brain data

Color codes and abbreviations for the custom regions used in Nutil Quantifier. These are consistent with the CCFv3-2017 nomenclature, except the three marked with an asterisk. Main titles correspond to high-level regions, whereas italic subtitles correspond to finer regions.

Midbrain. In the superior colliculus, a higher density was seen in the superficial (sensory related) part (1768 ± 257) than in deeper (motor related) layers (704 ± 238). The inferior colliculus (1352 ± 320) and the pretectal region (663 ± 209) also showed relatively high densities compared with other midbrain regions.

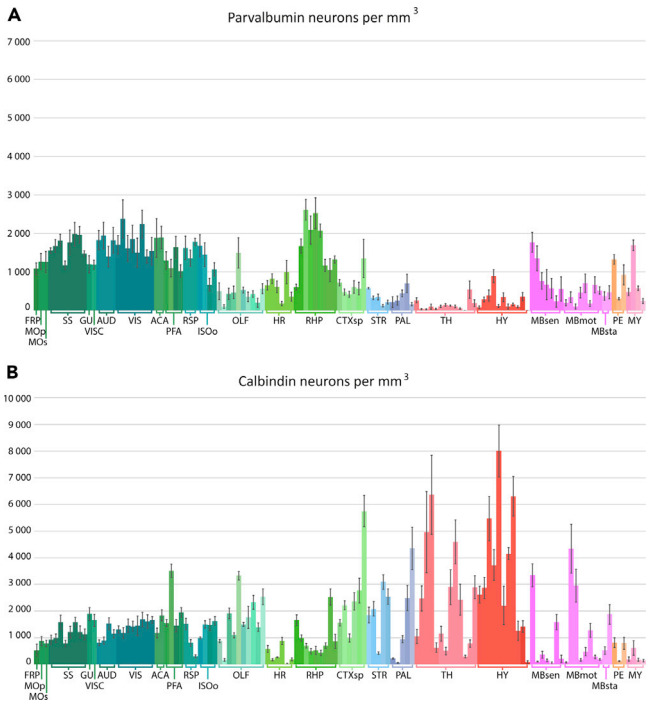

Figure 2. Parvalbumin and calbindin neuron densities across mouse brain regions

Bar graph showing the mean density per mm^3 of parvalbumin (n = 4; (A)) and calbindin (n = 5, (B)) neurons across the brain. Error bars indicate SEM. Groups of brain areas are indicated along the x axis. Bars are placed from left to right in the same order as abbreviations are listed and explained in Figure 1.

See Table S1 for an overview of all the density estimates.

Pons and medulla. Pontine and medullary regions were grouped into quite broad categories for the current analysis, but sensory related parts showed higher densities than the motor and behavioral state related ones (pons, sensory related: 1324 ± 126; medulla, sensory related: 1690 ± 140). Parvalbumin staining was seen across cerebellar layers, with Purkinje cell bodies darkly stained, but the staining was oversaturated, preventing extraction of cell numbers and densities.

Calbindin neuron densities across the mouse brain

Calbindin neurons were mapped and quantified throughout the mouse brain. In cortical areas, lightly stained but densely packed cells were typically seen in layer II, whereas deeper layers had a more scattered distribution of strongly stained cells. Density estimates for calbindin neurons in all regions are shown in Figure 2B.

Isocortex. Of the isocortical areas, the infralimbic area showed an especially high density (3506 ± 249), whereas the frontal pole showed a much more sparser distribution of calbindin neurons (532 ± 219). Within the primary somatosensory area, the trunk region showed the highest density (1582 ± 275), whereas the mouth region showed the lowest (782 ± 120). Densities were similar among the auditory and visual areas. Among retrosplenial areas, distinct differences were seen, with the ventral part having a lower density (306 ± 55) than the dorsal part (803 ± 130). The lateral agranular part of the retrosplenial cortex showed a higher density than both of these (1512 ± 218).

Olfactory areas. Olfactory areas showed a relatively high density of calbindin neurons, with an especially high density seen in the dorsal peduncular area (3324 ± 156). The accessory olfactory bulb, however, showed a very sparse distribution of calbindin neurons (164 ± 48).

Hippocampal formation. The hippocampal areas showed quite low calbindin neuron densities, with the dentate gyrus showing the highest density (876 ± 136). Retrohippocampal regions also generally showed low densities, except for the entorhinal area, lateral part with a moderate density (1659 ± 197), and the

hippocampo-amygdalar transition area, which showed a relatively high calbindin neuron density (2519 ± 303).

Cortical subplate. The claustrum and entopeduncular nucleus showed relatively high calbindin neuron densities, as did all amygdalar areas, except for the lateral amygdalar nucleus (986 ± 154). The density in the posterior amygdalar nucleus was considerably higher than all other subregions (5745 ± 589) of the cortical subplate.

Cerebral nuclei. Striatal regions generally showed relatively high densities of calbindin neurons, except for the olfactory tubercle that was very sparsely populated (418 ± 48). The caudoputamen had the highest total number of calbindin neurons of all brain regions (48064 ± 7665), but due to the large size of this region, the density was not considerably higher than other regions (1847 ± 295). However, we note that both the caudoputamen and striatum ventral region contained a large population of lightly stained cells, which as mentioned in the methods were not completely represented with our classifier. In the pallidum, quite low density was seen in the globus pallidus, both external (223 ± 24) and internal (57 ± 16) segments, whereas the ventral and medial regions of the pallidum showed a higher density, especially the latter (2492 ± 471).

Thalamus and hypothalamus. In the thalamus, especially high densities were seen in the subparafascicular nucleus (2474 ± 474) and the subparafascicular area (4964 ± 1526); the nuclei of the medial and midline groups in general had a high density of calbindin neurons. Hypothalamic regions showed relatively high densities of calbindin neurons, particularly the ventromedial hypothalamic nucleus (6298 ± 736) and medial preoptic nucleus (8003 ± 975).

Midbrain. The superficial layers of the superior colliculus, grouped under the sensory-related superior colliculus in the CCFv3-2017 hierarchy was densely packed with calbindin neurons (3345 ± 430). This was in contrast to a relatively sparse distribution in the motor-related superior colliculus (480 ± 148). In general, midbrain areas were quite lightly stained for calbindin with low cell densities revealed in our analysis, although some areas stood out as densely packed with cells. This included the midbrain trigeminal nucleus (2209 ± 863), ventral tegmental area (4339 ± 914), paranigral area (2951 ± 620), periaqueductal gray (1270 ± 262), and midbrain raphe nuclei (1872 ± 371).

Pons and medulla. Pontine and medullary regions generally showed low to moderate densities of calbindin neurons. In the cerebellum, intense staining was seen in the Purkinje cells; however, because these cells were much larger than calbindin neurons in the rest of the brain, we did not obtain a satisfactory segmentation, and quantitative data are not presented.

Different patterns of parvalbumin and calbindin neuron numbers in the mouse brain

We compared total number estimates of parvalbumin and calbindin neurons across the mouse brain. Results per region for each cell type are shown in Figure 3. This comparison shows that the parvalbumin neurons generally outnumber calbindin neurons in isocortical and retrohippocampal areas. In contrast, the striatal, olfactory, and cortical subplate areas generally had higher numbers of calbindin neurons. Striking differences were seen in the thalamus and hypothalamus, where parvalbumin neurons were sparse (<500 parvalbumin neurons per mm^3 across 10 out of 11 nuclei), whereas calbindin neurons showed high numbers in most subregions (>2000 calbindin cells per mm^3 in 8 out of 11 nuclei). In midbrain areas, and most notably in the inferior colliculus and parabigeminal nucleus, the number of parvalbumin neurons exceeded that of calbindin neurons. In the pons and medulla, parvalbumin neurons showed the highest numbers as well; however, as mentioned, we grouped these regions quite broadly, and more fine-grained analysis would be needed to determine if smaller pontine and medullary nuclei might show different ratios of the two cell types.

To further explore the ratios of parvalbumin and calbindin neurons across the brain, we created pie charts showing the total number estimates for each cell type per region in the CCFv3-2017 (Figure 4). The figure clearly shows the trend that parvalbumin neurons were relatively more abundant in isocortical areas, particularly in somatosensory and motor cortical areas. However, in prefrontal cortices, e.g. prelimbic (PL), infralimbic (ILA), and agranular insular (AGA) areas, the balance was shifted toward more calbindin neurons. Calbindin neurons were also more numerous in gustatory (GU) and visceral (VISC) cortices, intercalated between somatosensory and olfactory cortical areas. Areas of the hippocampal and retrohippocampal

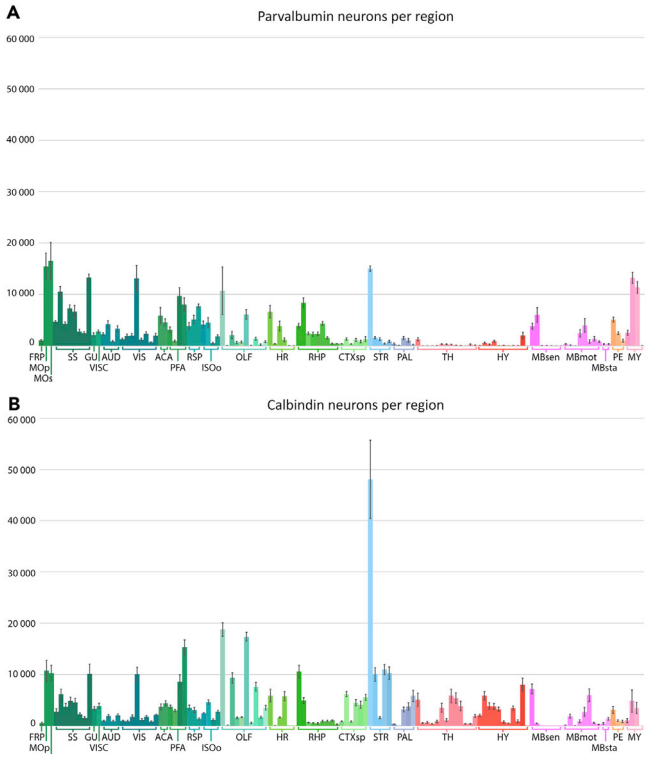

Figure 3. Comparison of total number estimates of parvalbumin and calbindin neurons across the mouse brain

Bar chart showing mean bilateral total number estimates of parvalbumin (n = 4; (A)) and calbindin (n = 5, (B)) neurons in mouse brain regions. Regions are defined and color coded according to the CCFv3-2017. Error bars indicate SEM. Groups of brain areas are indicated along the x axis. Bars are placed from left to right in the same order as abbreviations are listed and explained in Figure 1.

See Table S1 for an overview of all the total number estimates.

regions also showed higher parvalbumin than calbindin neuron numbers, with the exceptions of the dentate gyrus (DG), lateral entorhinal area (ENTl), and hippocampo-amygdalar transition areas (HATA). In olfactory, striatal, and cortical subplate areas, the calbindin neurons were more abundant. The dorsal pallidal regions had relatively equal (GPe) or higher parvalbumin numbers (GPi), whereas the ventral and medial pallidum showed higher numbers of calbindin neurons. All nuclei of the thalamus and hypothalamus showed a higher number of calbindin than parvalbumin neurons. In the midbrain, pons, and medulla, parvalbumin neurons were generally more abundant than calbindin neurons. However, the pedunculopontine nucleus (PPN), sensory superior colliculus (SCs), paranigral area (PN), ventral tegmental area (VTA), midbrain trigeminal nucleus (MEV), periaqueductal gray (PAG), and raphe nuclei (RAmb) stood out with high calbindin neuron numbers relative to parvalbumin neurons.

Comparative analysis of parvalbumin neurons in the rat and mouse hippocampal region

Parvalbumin neurons play an important role in the spatial circuits of the hippocampal region (Miao et al., 2017), where findings from rats and mice are often used interchangeably. To elucidate whether the parvalbumin neuron population in these species are similarly distributed within and across regions, we acquired immunohistochemical material showing parvalbumin neurons in the rat brain. We here compare the number, densities, and distributions of parvalbumin neurons in rat and mouse brain hippocampal regions. We focus on the hippocampal regions, as these are relatively similar among the two atlases used here (Kjonigsen et al., 2011; Wang et al., 2020). To facilitate comparison, we grouped regions in the CCFv3-2017 to their corresponding regions in the WHSv2 (Figures 5A and 5B). The brain regions mentioned in the following section are thus named according to the WHSv2 nomenclature and may differ slightly from CCFv3-2017 region terms used above. As collective terms, we use *hippocampal formation* to refer to regions of the Ammon's horn, dentate gyrus, fasciola cinereum and subiculum, and *parahippocampal region* for the pre- and parasubiculum and the entorhinal, perirhinal, and postrhinal cortices. These correspond to

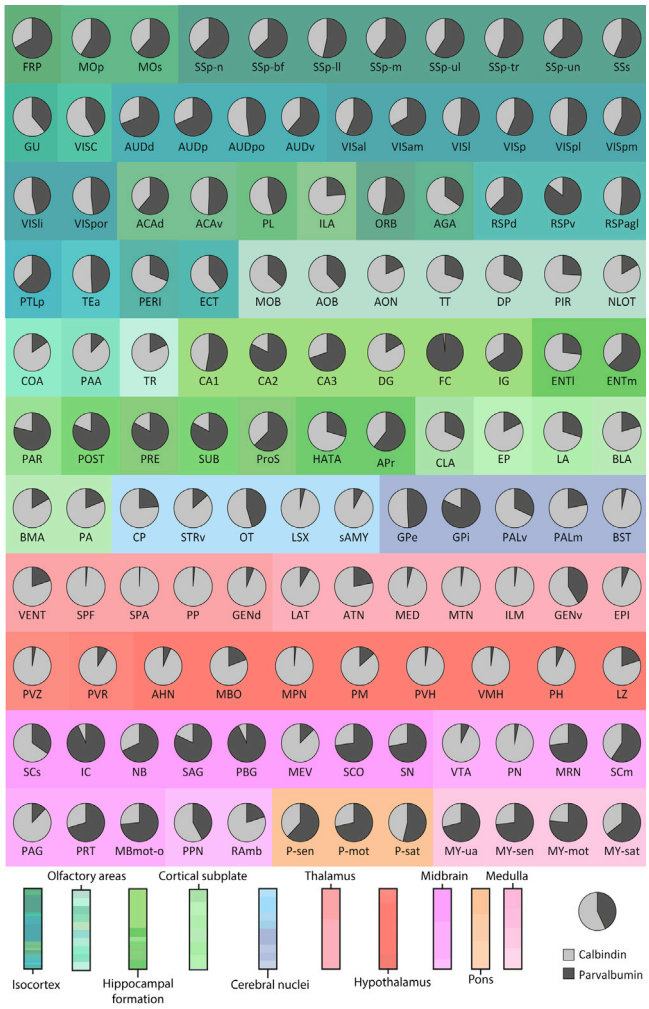

Figure 4. Ratios of parvalbumin and calbindin neurons across the mouse brain

Pie charts showing the ratio of each cell type (calbindin in light gray, parvalbumin in dark gray) across mouse brain areas. Abbreviations are detailed in Figure 1.

the collective terms hippocampal region and retrohippocampal region, respectively, in the CCFv3-2017. We use the term *hippocampal region* to refer to the hippocampal formation and parahippocampal region combined. Note that the medial entorhinal cortex is simply termed « entorhinal cortex» in WHSv2. We refer to it as medial entorhinal cortex in this manuscript, but it is called entorhinal cortex in the shared data files.

Quantitative estimates of parvalbumin neurons in the rat and mouse brain hippocampal regions. Our analysis of the hippocampal regions in the rat (n = 4) showed that the total number of parvalbumin neurons was highest in the medial entorhinal cortex (MEC; 20348 ± 4279), followed by cornu ammonis 1 (CA1; 18397 ± 1173), presubiculum (PrS; 15720 ± 1249), and subiculum (Sub; 13,804 ± 973). The highest density of parvalbumin neurons was seen in the PrS (1690 ± 134) and the parasubiculum (PaS; 1185 ± 125). The lateral entorhinal cortex (LEC) and dentate gyrus (DG) showed the lowest density of all subregions (LEC: 288 ± 62; DG: 231 ± 10). As in the rat, the mouse MEC had the highest number of parvalbumin neurons of all the hippocampal regions (8384 ± 940), followed by the CA1 (6631 ± 1221) and Sub (5898 ± 544). The density of parvalbumin neurons per mm^3 was highest in the PaS (2614 ± 269) and PrS (2306 ± 346). The least dense parvalbumin neuron population was seen in the LEC (607 ± 75) and DG (178 ± 56). All total number and density estimates for the hippocampal regions of the rat and mouse are summarized in Figures 5C and 5D.

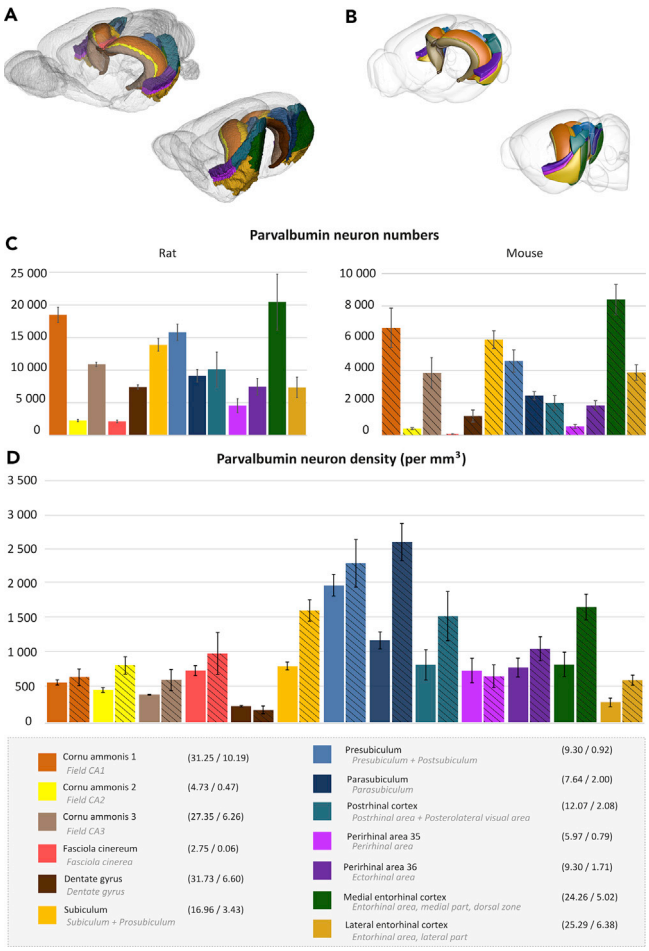

Figure 5. Cross-species comparison of parvalbumin neuron numbers and densities in hippocampal regions

(A) Rostrolateral and caudolateral (with cerebellum and brainstem removed) 3D views of the hippocampal regions in the WHSv2, shown in the color they are assigned in the atlas (Kjonigsen et al., 2015) within a transparent view of the brain.

(B) Corresponding 3D views of hippocampal regions in the CCFv3-2017. Regions are color coded according to their corresponding region in WHSv2.

(C and D) (C) Bar graphs showing the mean bilateral total number of parvalbumin neurons in rat (left) and mouse (right) brain hippocampal regions. (D) Bar graph showing the density per mm^3 of parvalbumin neurons in hippocampal regions. Solid bars show rat brain data and patterned bars show mouse brain data. Region names (WHSv2 terms in black text, corresponding CCFv3-2017 term in gray italic text), color codes according to WHSv2, and the volume (V) of each region (mouse/rat) are given in the lower panel. Error bars indicate SEM.

Thus, the estimated number of parvalbumin neurons was higher across all hippocampal regions of the rat brain as compared with the mouse—an expected finding given the relatively larger brain of the rat. In contrast, the density of parvalbumin neurons was generally higher in the mouse than in the rat (i.e. more parvalbumin neurons per mm^3). Regions within the hippocampal formation were relatively similar in parvalbumin neuron density: compared with mice, rats showed 11%–35% lower density in regions of Ammon's horn (CA1-3), 30% higher density in the DG, and 25% lower in the fasciola cinereum (FC). Larger differences were seen in the parahippocampal regions, particularly in the PaS, the POR, and the entorhinal cortices, with rats having 46%–55% lower density as compared with the mice.

The relative density among regions in the hippocampal formation (including in CA1-3, DG, Sub, and the FC) was retained across species, with the highest density seen in Sub, followed by relatively similar densities in CA1-3, and noticeably lower density in the DG. The same was true for the parahippocampal regions, where the PrS and PaS regions showed the highest density of parvalbumin neurons of all hippocampal regions, followed by the MEC, perirhinal areas, and POR.

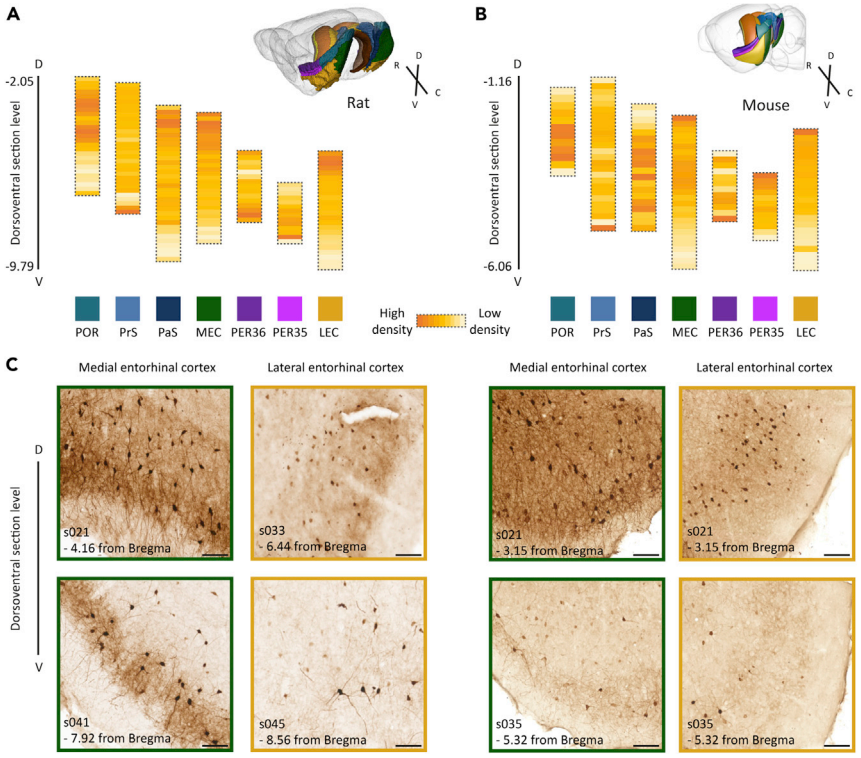

Figure 6. Parvalbumin neuron distribution along the dorsoventral axis of parahippocampal regions

(A and B) Colored bars, each representing one area of the parahippocampal region, with individual segments in each bar corresponding to a section along the dorsoventral axis. Approximate Bregma positions of sections along the dorsoventral axis are given. Parvalbumin neuron density is indicated by the intensity of the color (from light yellow to dark orange).|

(C) Example images from dorsal and ventral parts of the medial and lateral entorhinal cortex from rat (subject 25205, left panel) and mouse (subject 81266, right panel) showing a denser population of parvalbumin neurons in dorsal parts of these regions. Section numbers and approximate dorsoventral Bregma level are indicated for each image. Scale bars: 100 μm. Abbreviations: POR, postrhinal cortex; PrS, presubiculum; PaS, parasubiculum; MEC, medial entorhinal cortex; PER36, perirhinal area 36; PER35, perirhinal area 35; LEC, lateral entorhinal cortex.

Distribution of parvalbumin within mouse and rat brain hippocampal regions. Functional gradients are known to exist along the dorsoventral axis of the MEC (Brun et al., 2008; Giocomo et al., 2014) and in hippocampal-parahippocampal connectivity (Strange et al., 2014). We explored whether the density of parvalbumin neurons changed along the dorsoventral axis of each parahippocampal subregion. The results (summarized in Figure 6) indicated that the density of parvalbumin neurons decreases from dorsal to ventral levels in the POR, MEC, LEC, and PaS of the rat. We did not observe clear dorsoventral density gradients in the rat PrS or in the PER regions. In the mouse parahippocampal areas, the distribution of parvalbumin neurons decreased in the MEC and LEC, and a similar tendency was seen in perirhinal area 35 (PER35). No gradient was seen in the mouse PaS, but a dorsoventral increase in parvalbumin neuron density was observed in the mouse POR. However, this gradient was not seen when excluding the posterolateral visual area. In remaining areas, no clear gradients were observed (Figure 6).

Comparison of findings to earlier published data

We compared our estimates of parvalbumin neuron densities with the data presented by Kim et al. (2017) and with several other published reports (Figure 7). This comparison shows that our parvalbumin density estimates are generally lower than the ones provided by Kim et al. (2017). Differences between our estimates and those provided by Kim et al. (2017) were on average 57% in isocortical areas, 41% in olfactory areas, 38% in hippocampal regions, 35% in the cortical subplate, and 21% in the striatum. Larger differences were seen in the globus pallidus, small nuclei of the thalamus and hypothalamus, and in midbrain,

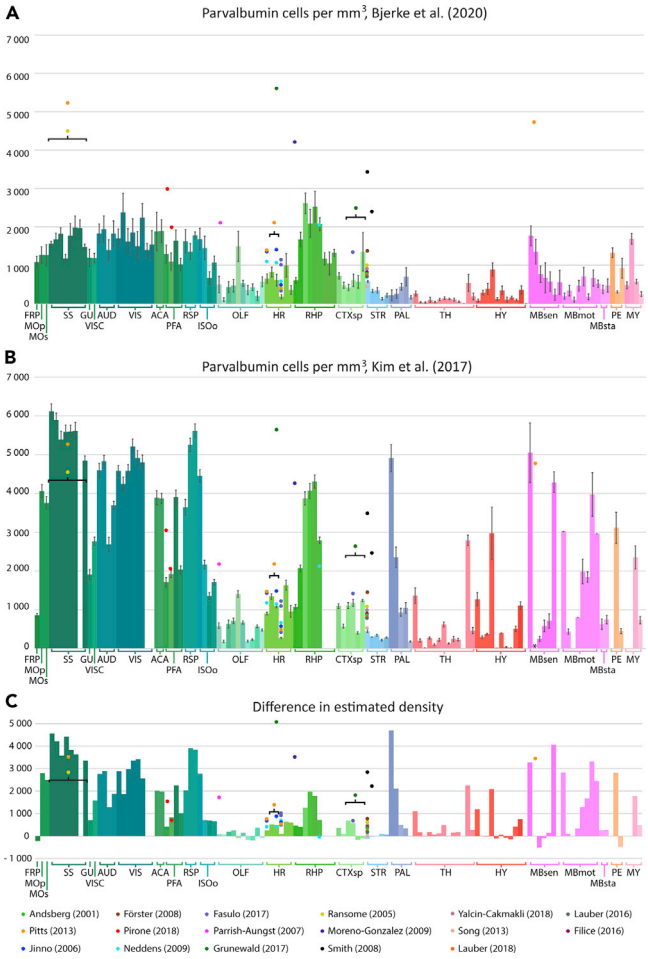

Figure 7. Comparison to previous reports

(A) Mean parvalbumin neuron density per mm^3 across the mouse brain reported here.

(B) Mean parvalbumin neuron density per mm^3 across the mouse brain as reported by Kim et al. (2017). Estimates (n = 32) found in 17 publications (listed below the bar graphs) are plotted in charts A and B according to the most closely matching region in the CCFv3-2017. Error bars indicate SEM.

(C) Difference in density estimates reported by Kim et al. (2017) and in the current study (values from current study subtracted from values reported by Kim et al. (2017)). Literature values are plotted according to their difference from the current study (values from the current study subtracted from the values from literature studies). Error bars indicate SEM. Abbreviations are detailed in Figure 1. Literature references: Andsberg et al. (2001); Ransome and Turnley (2005); Jinno and Kosaka (2006); Parrish-Aungst et al. (2007); Smith et al. (2008); Förster (2008); Moreno-Gonzalez et al. (2009); Neddens and Buonanno (2009); Pitts et al. (2013); Song et al. (2013); Filice et al. (2016); Lauber et al. (2016), 2018; Fasulo et al. (2017); Grünewald et al. (2017); Pirone et al. (2018); Yalcin-Cakmakli et al. (2018).

See Table S2 for detailed information on the literature sources.

pontine, and medullary nuclei where correspondence between atlas nomenclatures was poor. Still, many similar trends in the relative densities across regions can be seen in the datasets. We found 17 studies reporting parvalbumin neuron densities, in regions that could be mapped to closely corresponding region in the CCFv3-2017 atlas. Data for regions that could not be interpreted relative to the CCFv3-2017 atlas were not included in our comparison. Thirty-two estimates of parvalbumin densities were compared with our findings. The majority of these (19 of 32 estimates), mainly from hippocampal and striatal brain regions, were relatively well aligned with our density estimates, whereas the remaining ones (13 of 32 estimates) were considerably higher than the here reported estimates. All these studies used immunohistochemistry or fluorescence with antibodies targeting parvalbumin. A more detailed comparison (including information about strains, regions, and antibodies used in each study) can be found in Table S2, and

similar comparison data for rat parvalbumin and mouse calbindin neurons can be found in Tables S3 and S4, respectively.

Validity of QUINT results

Results obtained with the QUINT workflow critically depend on the validity of the segmentations used for quantification. To validate the numbers obtained using QUINT, i.e. counts of labeled neurons automatically detected using ilastik (below referred to as QUINT counts), we compared them with numbers obtained using manual identification of neurons (below referred to as manual counts).

Parvalbumin-stained material

We first compared numbers of parvalbumin positive neurons obtained in one hemisphere from one section and found that QUINT gave 9% higher counts in the neocortex (manual count = 2,175; QUINT count = 2379), 3% higher counts in the hippocampal and parahippocampal regions (manual count = 540, QUINT count = 555), and 15% higher counts in striatal and pallidal regions (manual count = 295, QUINT count = 340).

Secondly, we compared numbers obtained from the medial entorhinal cortex (23 sections) and found that QUINT provided a 5% higher total number of parvalbumin-positive neurons counted (manual count = 3,400; QUINT count = 3,560). Using Abercrombie's formula to correct for double-counting and multiplying by the section interval, the total number estimates in the unilateral medial entorhinal cortex were 14,836 using manual counts and 15,535 using QUINT counts.

For individual sections from the entorhinal cortex, we found the difference between QUINT counts and manual counts to be on average 5.5% (ranging from 0%–16% difference) between the two approaches. QUINT counts were generally higher than manual counts (in 21 of 23 sections), and the degree of difference was not associated with whether or not sections were used to train the ilastik segmentation algorithm (on average 5% difference in training sections and 6% difference in non-included sections). The results from both methods per section are summarized in Figure S1. By qualitative comparison of manually identified neurons and ilastik segmentations, we observed that the differences were mainly due to inclusion of labeled objects that were not cells (e.g. clustered neuropil) in the ilastik segmentation. In our main analysis, we therefore added a manual step to remove such erroneously segmented objects (see Transparent Methods for details).

Calbindin-stained material

We compared QUINT and manual counts of calbindin-positive neurons in one hemisphere in one section. QUINT counts were 10% higher in cortical regions (manual count = 654, QUINT count = 719) as well as in striatal and pallidal regions (manual count = 1,371, QUINT count = 1,513), whereas 2% lower in the hypothalamus (manual count = 98, QUINT count = 96). In olfactory regions, QUINT counts were 44% higher than the manual counts (manual count = 63, QUINT count = 91). We finally compared QUINT and manual counts of calbindin neurons in the anterior cingulate cortex and found that QUINT counts were 16% higher than manual counts (manual count = 905, QUINT count = 961). As for the parvalbumin data, we manually removed erroneously segmented objects from the calbindin image segmentations in our main analysis.

Reliability of QUINT results

Intrarater reliability. To assess the intrarater reliability of the segmentations, one researcher trained three ilastik classifiers based on identical material to generate three sets of segmentations. Variability was very low in the hippocampus and parahippocampal areas (1%–3% difference) and neocortex (0.2%–2% difference); relatively low in the striatum (3%–10% difference), globus pallidus (1%–8% difference), and hypothalamus (10%–11% difference); and slightly higher in the substantia nigra (8–14% difference) and basal forebrain (3–13% difference). Results from the intrarater reliability test for all regions are summarized in Figure S2, and all the derived data are included in Data 1. The variability seemed independent of the time interval (a few days or six weeks) between the timing of the classifiers (Figure S2).

Interrater reliability. We assessed the interrater reliability of the segmentation results by presenting five researchers with the same material and the same instructions for segmentation. All the segmentations were then analyzed with the QUINT workflow based on identical atlas maps and the results compiled for major

brain regions. Interrater reliability for these regions ranged from 8%–29% for the different researchers (see Data 1 and Figure S3 for a summary of the quantitative and qualitative results).

The segmentations generated by each researcher either consistently over- or underestimated the number of objects relative to the original segmentations that were used to produce the instructions, with the exception of two regions from one of the researchers. Qualitatively, we observed that the segmentations that underestimated objects relative to the original segmentation often did not extract the most "extreme" cases of labeling, i.e. very darkly stained cells or light-to-medium stained cells. The documentation instructed not to segment very light cells, which might have left room for interpretation in such cases.

To train pixel classifiers in ilastik, classes are created and example annotations applied to the image for each class. We exported and quantified the annotations placed by each researcher with the QUINT workflow using the default custom regions in Nutil Quantifier for the WHS atlas. The original classifier contained 90 annotated objects for the "cell" class, whereas the classifiers created as part of the interrater reliability study contained 33–63 annotations for this class. All the researchers placed "cell" annotations in the cortex and hippocampus, with all but one placing annotations in the olfactory and striatal/pallidal regions. For the "background" class, all the researchers placed annotations in the cortex, fiber tracts, and hippocampus, with most placing annotations in the olfactory regions as well. As the documentation instructed the researchers to place annotations in all these regions, there was some variability in the compliance to the segmentation instructions.

Discussion

We have quantified densities and numbers of immunolabeled calbindin and parvalbumin neurons across the entire mouse brain using the QUINT workflow (Yates et al., 2019), which combines interactive machine-learning-based image segmentation with regions of interest defined using 3D anatomical references atlases. We also quantified parvalbumin neurons in the rat brain. We provide the first brain-wide quantitative analysis on the distribution of immunolabeled calbindin and parvalbumin cells. Below, we first discuss the efficiency, validity, and reproducibility of our methodology, with particular focus on our comparison to the literature, before elaborating on the quantitative results. Lastly, we discuss how open sharing of the different (raw and derived) components of our datasets may facilitate their re-use in new analyses.

Our methodology allows semi-automatic quantification of the numbers and densities of labeled neurons across the brain. The use of an open access 3D reference atlas makes it easier to compare data across studies, and open sharing of the different components of the datasets facilitates re-interpretation of results with different methods. The considerable variability in neuron numbers across the literature (Keller et al., 2018) and the challenges related to interpret the causes of such discrepancies (see, e.g. Bjerke et al., 2020a) highlights the need for re-usable data and transparent analyses. Additional studies will be needed to accumulate quantitative evidence about normal inter-individual variability.

We here used antibodies specific for parvalbumin or calbindin-expressing neurons, which have broad interest for their calcium-buffering capacities (Schwaller, 2020) and functional roles in various neural networks (Atallah et al., 2012; Li et al., 2017; Miao et al., 2017). Although immunohistochemistry is useful for mapping the distribution of cell types across entire brains, our protocol did not allow classification of cell subtypes. Subtypes are typically identified using combinations of morphological, electrophysiological, or hodological characteristics (see, e.g. Ascoli et al., 2008; Ibáñez-Sandoval et al., 2010). Our findings thus reflect broad classes of neurons, but does not distinguish cellular subtypes such as parvalbumin expressing basket or chandelier cells (Tremblay et al., 2016; Wang et al., 2019). Further studies are needed to map the distribution of finer neuronal subclasses. The QUINT workflow (Yates et al., 2019) is well suited for future studies replicating our findings and adding data for other markers, e.g. to address questions of variability within or across different strains, sex, or age groups. An important premise for such future comparisons is the use of the same anatomical reference atlas.

We have shown that the profile counts obtained with the QUINT workflow are in accordance with manual counts from the same areas. To further improve our ilastik segmentations, we implemented a post-processing step for the manual removal of erroneously segmented objects. To convert profile counts into cell number estimates for entire regions, it is necessary to address several sources of bias (Attili et al., 2019). First,

when the brain is cut into sections, some cells are split and can therefore appear in more than one section, which may lead to overcounting. We corrected for this by using Abercrombie's formula (Abercrombie, 1946). Secondly, cells that are located at the border between two atlas regions must only be counted one. To ensure this, we switched off the "object splitting" feature in Nutil Quantifier to assign objects to one region only. Third, the bias of lost caps (i.e. cell fragments at the edges of a section may be "lost" or invisible; Hedreen, 1998) are inherent to profile counts in histological material. Correcting for this would require estimating a factor based on the observed number of profiles and the true number of cells, the latter that cannot be derived from section images. Lastly, cells located in deeper parts of a thick section may be occluded by those in the upper layer. Correcting for this would require dividing the section into layers along the z axis, which is also not possible in section images. Although we did not address these last two sources of bias, it has been shown that profile counting with Abercrombie's correction yields similar results to both stereology and three-dimensional reconstruction of entire cell populations (Baquet et al., 2009). Thus, to the extent to which our QUINT profile counts accurately reflect manual profile counts, we also consider them to reflect cell counts when corrected and multiplied to represent whole regions.

Our interrater reliability testing indicated that detailed instructions on the criteria for segmentation, with visualization of the expected outcome, can be effective in allowing researchers to recreate an analysis. In this test, only one parameter (the ilastik segmentations) was different between the researchers. In contrast, reproducibility of scientific findings is typically evaluated across scientific papers where the sources of variability may be many and hard to assess. Although methods sections in scientific reports are intended to provide sufficient and necessary details to reproduce results, they often lack critical information needed to interpret analyses (Bjerke et al., 2018; Keller et al., 2018). Our instructions were formulated as a stepwise procedure and may not be representative of a typical methods section, but we believe it can give clues to the details that are important for researchers to interpret and recreate an analysis. For documentation of counts, several visual examples of what is considered an object should be considered a minimum. Ideally, representations of objects across the entire material (such as the segmentation images provided here) allows other researchers to gain a deeper understanding of the analytic results.

We compared our brain-wide data on parvalbumin neuron densities with those provided by Kim et al. (2017) and found the densities obtained by Kim et al. (2017) to align well with our data in hippocampal and striatal regions, as well as in many thalamic and hypothalamic regions. Small differences can likely be ascribed to different definitions of the individual areas. Because Kim et al. (2017) employed a custom, 3D reconstructed version of the Allen Reference Atlas (Dong, 2008; Kim et al., 2015), we were not able to reliably compare data from all regions in their atlas version and ours. Significant changes were made to cortical and hippocampal delineations in the CCFv3-2017 delineations (Wang et al., 2020), and nomenclature differences in brainstem regions indicate that delineations in these regions have changed as well. For isocortical regions, however, Kim et al. (2017) reported density estimates that were much higher than ours across almost all regions. These differences are not likely to be caused only by different definitions of subregions. Although we used immunohistochemistry, Kim et al. (2017) employed Cre-reporter mice expressing fluorescent protein in parvalbumin neurons. As the two methods will visualize cells that express the parvalbumin protein and parvalbumin gene, respectively, our lower estimates could be caused by cells having only transient production of the protein, e.g. during development (Madisen et al., 2010) or variable expression levels associated with environmental/behavioral circumstances (Donato et al., 2013). Such cells would be detected by the Cre-reporter approach used by Kim et al. (2017) but not by immunohistochemistry as used in our study. Differences in segmentation and quantification methods may of course also influence results. Despite differences in data acquisition and analysis, similar trends in the relative densities of cells were seen across brain regions in the two datasets.

We also gathered quantitative estimates from the literature to benchmark our reported values. However, many studies report two- or three-dimensional densities based on one or a few sections that are unlikely to be representative for an entire region. Furthermore, regional areas or volumes estimated from sections will be highly affected by tissue shrinkage occurring during immunohistochemical procedures (Dorph-Petersen et al., 2001), and few studies report the use of shrinkage correction factors. In our analysis, we used the region volumes from the three-dimensional reference atlas, based on serial two-photon tomography and magnetic resonance imaging templates (for mouse and rat brain atlases, respectively). These are less affected by shrinkage than histological section material, which will result in estimated densities being lower. Given the large effects of tissue shrinkage on density estimates, it has been argued that total number

estimates should preferentially be acquired and reported (Oorschot, 1994), but we observe that density estimates are more often reported in the literature. We note that the cell diameter measurement used in Abercrombie's formula in the current study will also be affected by tissue shrinkage, which will to some degree affect our total number estimates. Nevertheless, in the few cases where we found total number estimates from stereological studies with regions of interest closely corresponding to those used in our analysis (Andsberg et al., 2001; Filice et al., 2016; Lauber et al., 2016, 2018), we observed a high degree of correspondence with our total number estimates. This indicates that our estimates using Abercrombie's formula is not severely biased by the cell diameter approximation used here. Furthermore, for the literature sources that gave estimates from more than one region of interest, the same trend was seen across regions as in our data. We thus believe that the comparison of our parvalbumin data to those provided by Kim et al. (2017) taken together with those found in the other non-whole brain studies mentioned above indicates that our estimates reveal reproducible trends across regions.

For calbindin neurons in the mouse, very few quantitative estimates were available from the literature, some of which corresponded well to ours and some of which provided much higher numerical values. We note that a subset of calbindin neurons is very lightly stained (in accordance with previous observations, see Frantz and Tobin (1994)). The classifier used in our segmentation successfully extracted calbindin neurons of high and medium staining intensity but did not extract the most lightly stained neurons, thus our estimates might be considered lower bounds. Lightly stained neurons were seen across the brain but were most abundant in layer II of isocortical areas, in the striatum, the dentate gyrus, and hypothalamus. To extract these neurons, it might be necessary to train separate classifiers for different areas, perhaps also using images of higher resolution than used here. However, very light cells may be hard to distinguish from background staining also for a trained neuroanatomist.

Our comparison of calbindin and parvalbumin neuron numbers across the mouse brain revealed largely complementary patterns, possibly indicating differences in the relative contribution of these cell types within regions and across systems. The distribution of cells types, neurotransmitter receptors, and axonal connections varies substantially across different cortical and subcortical areas (see, e.g. Awasthi et al., 2020; Yu et al., 2019b). Such diversity occurs at multiple levels, from microcircuits to large-scale patterns across brain areas (Caroni, 2015; Kim et al., 2017), and specific combinations of multiple neurotransmitter receptors and cell types have been proposed to underlie specific functional characteristics of regions and networks (Zilles et al., 2015). In line with this, our findings show that parvalbumin neurons are more abundant in motor and sensory areas as well as in most of the hippocampal region, whereas calbindin neurons are dominant in limbic and hypothalamic areas. The importance of parvalbumin neurons in sensory-motor cortical areas was also highlighted by Kim et al. (2017), who found parvalbumin neurons to be the dominant among three interneuron types in these areas. They further found somatostatin-positive neurons to be the most prevalent interneuron type in cortical frontal and association areas. Calbindin may be expressed in subsets of somatostatin and vasointestinal protein expressing (VIP) neurons, which together with parvalbumin neurons make up almost all the interneurons in the neocortex (Rudy et al., 2011). However, calbindin is also known to be expressed in principal neurons, e.g. pyramidal cells in the CA1 (Merino-Serrais et al., 2020) and medial entorhinal cortex (Ohara et al., 2019; Ray et al., 2014). The thalamus also showed high numbers of calbindin neurons compared with parvalbumin positive ones. Given the recent finding that most thalamic nuclei have a very sparse GABAergic population (Evangelio et al., 2018), it is likely that the numerous calbindin neurons in the thalamus are excitatory principal neurons. In the midbrain, we found parvalbumin neurons to be dominant in sensory and motor-related regions such as the inferior colliculus, nucleus sagulum, parabigeminal nucleus, and substantia nigra, whereas calbindin was more prevalent in regions involved in behavioral state regulation and pain modulation, such as the periaqueductal gray, ventral tegmental area, and midbrain raphe nuclei. Thus, although calbindin-expressing neurons may represent both principal neurons and interneurons depending on the area in question, we observe that they generally seem to be most numerous in subcortical areas related to emotional processing and behavioral state regulation. Kim et al. found increased numbers of somatostatin and VIP neurons in several subcortical areas of female mice. Although our sample size of each sex in this study was insufficient to approach questions about sexual dimorphism, future studies may build on our material to allow such analyses. Together, our observations provide a neuroanatomical underpinning for recent evidence supporting the importance of calbindin neurons in social and anxiety-like behavior (Harris et al., 2016) and their susceptibility to stressful events (Li et al., 2017) and supports the already emphasized role of parvalbumin neurons in sensory systems and spatial navigation (Atallah et al., 2012; Miao et al., 2017; Runyan et al., 2010; Yu et al., 2016, 2019a).

In our cross-species comparison of parvalbumin neurons in the hippocampal region, we generally found higher parvalbumin neuron densities in mice than in rats, which is consistent with earlier reports of mice having lower total numbers but higher densities of neurons across the brain than rats (Herculano-Houzel et al., 2006). In both species, the density of parvalbumin neurons decreased from dorsal to ventral in the entorhinal cortex. This observation correlates with the increasing scaling of grid cell firing fields along the dorsoventral axis of the MEC (Brun et al., 2008; Stensola et al., 2012). Cells in the LEC have been found to be tuned to object positions and can coordinate to encode time information (Tsao et al., 2013, 2018), although the relationship between their properties and position along the dorsoventral axis is less well defined. A decreasing gradient in the inhibitory input from parvalbumin interneurons has been described from dorsal to ventral in the entorhinal cortex of mice (Beed et al., 2013; Kobro-Flatmoen and Witter, 2019), and dorsoventral gradients in the number of cell bodies have been described qualitatively in the LEC and MEC of adult mice (Fujimaru and Kosaka, 1996). Our evidence of a dorsal to ventral parvalbumin neuron density gradient in the MEC of both rats and mice correlates well with these connectional and functional gradients, and we show similar trends in the LEC as well. Recent research has indeed highlighted the possibility that similar principles govern the microcircuit wiring in MEC and LEC (Nilssen et al., 2018). Our results indicate that a decreasing dorsoventral density of parvalbumin interneurons may be one such principle.

Similarly, a decreasing density of parvalbumin neurons was seen from dorsal to ventral in the rat PaS and POR. The mouse POR did not show a dorsoventral decrease in parvalbumin neuron density; if anything, there was an opposite trend with increasing densities from dorsal to ventral. However, caution is warranted when interpreting this result, as no gradient was seen when excluding the region termed posterolateral visual area in the CCFv3-2017 from our definition of the mouse POR. A dorsoventral decrease in density was seen in the mouse PER35, although this gradient was not as clear as for the other areas mentioned. Several of the parahippocampal regions show a similar trend of decreasing parvalbumin neuron densities from dorsal to ventral, a trend that seemed more wide-spread in the rat. In conclusion, we show that parvalbumin neurons distribute according to similar principles in rat and mice hippocampal regions. Whether smaller differences between the species would persist across a larger sample and ultimately reflect functional specializations in rats and mice is a topic for future studies, but it should be noted that different configurations in a network might not necessarily critically affect function (Marder et al., 2015).

We share segmentation results together with the primary data from which they were derived. In addition to increasing transparency of analysis, this facilitates re-use and re-analysis of the derived data. For example, when new versions of the Waxholm Space rat brain atlas or the Allen Mouse Brain atlas are published, our segmentation images can be reanalyzed with new atlas maps. Thus, beyond the quantitative derived data presented here, we consider both the primary data and the segmentation maps to be re-usable for the community in the long term.

In conclusion, we here present numbers and distributions of parvalbumin and calbindin neurons across the mouse brain. We compare our results to previously published estimates, showing that our estimates of parvalbumin neurons across the mouse brain are well aligned with a previous brain-wide analysis (Kim et al., 2017) and the literature in striatal and hippocampal regions, where several studies have reported quantitative data. However, in other brain regions, larger differences were seen and very few studies were available. Direct comparisons are typically impeded by lack of information in publications, thus highlighting the need for transparent analyses and their reproduction. Furthermore, we compare the number and distribution of parvalbumin neurons in the mouse hippocampal region with similar data from the rat. Our analysis of parvalbumin and calbindin neurons points to trends within and across brain regions and species that align well with previous studies showing functional and connectional organization of these cell types.

Limitations of the study

The limitations of our study are discussed at length in the main text. Notably, use of immunohistochemistry to identify parvalbumin and calbindin neurons may lead to different results than obtained with other methods for visualization of cells (e.g. the use of transgenic animals). Our method reveals broad cell classes and does not allow identification of subtypes such as parvalbumin positive basket and chandelier cells. Our use of atlas registration and semi-automated image analysis allowed efficient quantification across the

brain, but the classification method did not necessarily capture all cells (e.g. lightly stained calbindin neurons). Results obtained should always be interpreted in light of the methodological approach, which might underlie some of the differences seen among studies in our comparison to the literature.

Resource availability

Lead contact

For further information and requests for resources and reagents contact corresponding author, Trygve B. Leergaard (t.b.leergaard@medisin.uio.no).

Materials availability

This study did not generate new unique reagents.

Data and code availability

All raw and derived data from this project are shared via the EBRAINS research infrastructure (https://ebrains.eu/). The primary datasets contain high-resolution TIFF images of the immunohistochemical material and are shared under the following titles:

1) Distribution of calbindin-positive neurons in the normal adult mouse brain (Bjerke and Leergaard, 2020)
2) Distribution of parvalbumin-positive interneurons in the normal adult mouse brain (Laja et al., 2020a)
3) Distribution of parvalbumin-positive interneurons in the normal adult rat brain (Laja et al., 2020b)

The derived datasets contain downscaled PNG images of the primary data, PNG images for the segmentations, atlas maps (PNG and FLAT files), NUT files used to run Nutil Quantifier and all the output reports from this analysis, as well as the final quantitative results per region of interest as presented in this paper. The derived datasets are shared under the following titles:

1) Brain-wide quantitative data on calbindin-positive neurons in the mouse (Bjerke et al., 2020b)
2) Brain-wide quantitative data on parvalbumin-positive neurons in the mouse (Bjerke et al., 2020c)
3) Brain-wide quantitative data on parvalbumin-positive neurons in the rat (Bjerke et al., 2020d)

Together, the material provided in the derived dataset allows other researchers to re-run the analysis performed here, re-use the segmentation files with other atlas maps or other parameters in Nutil Quantifier, or re-segment the image material.

Methods

All methods can be found in the accompanying Transparent Methods supplemental file.

Supplemental information

Supplemental Information can be found online at https://doi.org/10.1016/j.isci.2020.101906.

Acknowledgments

We thank Ingrid Reiten and Kasper Kjelsberg for help with the reliability studies; Nicolaas Groeneboom, Grazyna Babinska, and Hong Qu for expert technical assistance; and Heidi Kleven and Martin Øvsthus for useful discussions. This work was funded by the European Union's Horizon 2020 Framework Programme for Research and Innovation under the Specific Grant Agreement No. 785907 (Human Brain Project SGA2), Specific Grant Agreement No. 945539 (Human Brain Project SGA3), and The Research Council of Norway under Grant Agreement No. 269774 (INCF Norwegian Node). The experimental work done in Kavli Center was supported by the Research Council of Norway Grant 227769, the Kavli Foundation, the Center of Excellence scheme of the Research Council of Norway-Centre for Neural Computation Grant 223262, and the National Infrastructure scheme of the Research Council of Norway-NORBRAIN Grant 197467. High-resolution digital images were acquired using infrastructure established through the Norwegian Brain Initiative, NORBRAIN, supported by Research Council of Norway Grant 295721.

Authors contribution

IEB conceived the study, performed the immunohistochemical processing and analysis, organized and prepared the related datasets for sharing, and composed the manuscript with comments from all authors. SCY contributed to designing of the data analysis and validity testing and prepared the analytical workflows. AL performed immunohistochemical processing and contributed to organizing related datasets. MPW contributed to supervising the study. MAP supervised the designing of the data analysis and the development of the analytical workflows. JGB supervised the development of the analytical workflows. TBL conceived and supervised the study and the writing of the manuscript. All authors contributed to conceiving the study and the writing the manuscript. All authors reviewed and approved the final manuscript.

Declaration of interests

The authors declare no competing interests.

Received: July 27, 2020
Revised: September 30, 2020
Accepted: December 3, 2020
Published: January 22, 2021

References

Abercrombie, M. (1946). Estimation of nuclear population from microtome sections. Anat. Rec. *94*, 239–247.

Andsberg, G., Kokaia, Z., and Lindvall, O. (2001). Upregulation of p75 neurotrophin receptor after stroke in mice does not contribute to differential vulnerability of striatal neurons. Exp. Neurol. *169*, 351–363.

Arai, R., Jacobowitz, D., and Deura, S. (1994). Distribution of calretinin, calbindin-D28k, and parvalbumin in the rat thalamus. Brain Res. Bull. *33*, 595–614.

Ascoli, G., Alonso-Nanclares, L., Anderson, S., Barrionuevo, G., Benavides-Piccione, R., Burkhalter, A., Buzsáki, G., Cauli, B., Defelipe, J., Fairén, A., et al. (2008). Petilla terminology: nomenclature of features of GABAergic interneurons of the cerebral cortex. Nat. Rev. Neurosci. *9*, 557–568.

Atallah, B., Bruns, W., Carandini, M., and Scanziani, M. (2012). Parvalbumin-expressing interneurons linearly transform cortical responses to visual stimuli. Neuron *73*, 159–170.

Attili, S., Silva, M., Nguyen, T.-V., and Ascoli, G. (2019). Cell numbers, distribution, shape, and regional variation throughout the murine hippocampal formation from the adult brain Allen Reference Atlas. Brain Struct. Funct. *224*, 2883–2897.

Awasthi, J.R., Tamada, K., Overton, E.T.N., and Takumi, T. (2020). Comprehensive topographical map of the serotonergic fibers in the male mouse brain. J. Comp. Neurol. 1–39, https://doi.org/10.1002/cne.25027.

Baquet, Z., Williams, D., Brody, J., and Smeyne, R. (2009). A comparison of model-based (2D) and design-based (3D) stereological methods for estimating cell number in the substantia nigra pars compacta (SNpc) of the C57BL/6J mouse. Neuroscience *161*, 1082–1090.

Beed, P., Gundlfinger, A., Schneiderbauer, S., Song, J., Böhm, C., Burgalossi, A., Brecht, M., Vida, I., and Schmitz, D. (2013). Inhibitory gradient along the dorsoventral axis in the medial entorhinal cortex. Neuron *79*, 1197–1207.

Berg, S., Kutra, D., Kroeger, T., Straehle, C., Kausler, B., Haubold, C., Schiegg, M., Ales, J., Beier, T., Rudy, M., et al. (2019). Ilastik: interactive machine learning for (bio)image analysis. Nat. Methods, 1226–1232.

Berridge, M. (1998). Neuronal calcium signaling. Neuron *21*, 13–26.

Bezaire, M.J., and Soltesz, I. (2013). Quantitative assessment of CA1 local circuits: knowledge base for interneuron-pyramidal cell connectivity. Hippocampus *23*, 751–785.

Bjerke, I., and Leergaard, T. (2020). Distribution of calbindin positive neurons in the normal adult mouse brain. EBRAINS. https://doi.org/10.25493/KHNT-KV8.

Bjerke, I., Øvsthus, M., Andersson, K., Blixhavn, C., Kleven, H., Yates, S., Puchades, M., Bjaalie, J., and Leergaard, T. (2018). Navigating the murine brain: toward best practices for determining and documenting neuroanatomical locations in experimental studies. Front. Neuroanat. *12*, 1–15.

Bjerke, I., Puchades, M., Bjaalie, J., and Leergaard, T. (2020a). Database of literature derived cellular measurements from the murine basal ganglia. Sci. Data *7*, 211.

Bjerke, I., Yates, S., Puchades, M., Bjaalie, J., and Leergaard, T. (2020b). Brain-wide quantitative data on calbindin positive neurons in the mouse. EBRAINS. https://doi.org/10.25493/TT2Y-23N.

Bjerke, I., Yates, S., Puchades, M., Bjaalie, J., and Leergaard, T. (2020c). Brain-wide quantitative data on parvalbumin positive neurons in the mouse. EBRAINS. https://doi.org/10.25493/BT8X-FN9.

Bjerke, I., Yates, S., Puchades, M., Bjaalie, J., and Leergaard, T. (2020d). Brain-wide quantitative data on parvalbumin positive neurons in the rat. EBRAINS. https://doi.org/10.25493/KR92-C33.

Boccara, C.N., Kjonigsen, L.J., Hammer, I.M., Bjaalie, J.G., Leergaard, T.B., and Witter, M.P. (2015). A three-plane architectonic atlas of the rat hippocampal region. Hippocampus *25*, 838–857.

Brun, V.H., Solstad, T., Kjelstrup, K.B., Fyhn, M., Witter, M.P., Moser, E.I., and Moser, M.B. (2008). Progressive increase in grid scale from dorsal to ventral medial entorhinal cortex. Hippocampus *18*, 1200–1212.

Caroni, P. (2015). Inhibitory microcircuit modules in hippocampal learning. Curr. Opin. Neurobiol. *35*, 66–73.

Couey, J.J., Witoelar, A., Zhang, S.J., Zheng, K., Ye, J., Dunn, B., Czajkowski, R., Moser, M.B., Moser, E.I., Roudi, Y., et al. (2013). Recurrent inhibitory circuitry as a mechanism for grid formation. Nat. Neurosci. *16*, 318–324.

Donato, F., Rompani, S.B., and Caroni, P. (2013). Parvalbumin-expressing basket-cell network plasticity induced by experience regulates adult learning. Nature *504*, 272–276.

Dong, H. (2008). Allen Reference Atlas: A Digital Color Brain Atlas of the C57BL/6J Male Mouse (John Wiley & Sons).

Dorph-Petersen, K.-A., Nyengaard, J.R., and Gundersen, H.J.G. (2001). Tissue shrinkage and unbiased stereological estimation of particle number and size. J. Microsc. *204*, 232–246.

Evangelio, M., García-Amado, M., and Clascá, F. (2018). Thalamocortical projection neuron and interneuron numbers in the visual thalamic nuclei of the adult C57BL/6 mouse. Front. Neuroanat. *12*, 27.

Fasulo, L., Brandi, R., Arisi, I., La Regina, F., Berretta, N., Capsoni, S., D'Onofrio, M., and Cattaneo, A. (2017). ProNGF drives localized and

cell selective parvalbumin interneuron and perineuronal net depletion in the dentate gyrus of transgenic mice. Front. Mol. Neurosci. *10*, 20.

Ferguson, B., and Gao, W. (2018). PV interneurons: critical regulators of E/I balance for prefrontal cortex-dependent behavior and psychiatric disorders. Front. Neural Circuits *12*, 1–13.

Filice, F., Vörckel, K.J., Sungur, A.Ö., Wöhr, M., and Schwaller, B. (2016). Reduction in parvalbumin expression not loss of the parvalbumin-expressing GABA interneuron subpopulation in genetic parvalbumin and shank mouse models of autism. Mol. Brain, 1–17.

Förster, J. (2008). Quantitative Morphological Analysis of the Neostriatum and the Cerebellum of Tenascin-C Deficient Mice (University of Hamburg), Thesis. http://citeseerx.ist.psu.edu/viewdoc/download?doi=10.1.1.427.6474&rep=rep1&type=pdf.

Frantz, G., and Tobin, A. (1994). Cellular distribution of calbindin D28K mRNAs in the adult mouse brain. J. Neurosci. Res. *37*, 287–302.

Fujimaru, Y., and Kosaka, T. (1996). The distribution of two calcium binding proteins, calbindin D-28K and parvalbumin, in the entorhinal cortex of the adult mouse. Neurosci. Res. *24*, 329–343.

Giocomo, L., Stensola, T., Bonnevie, T., Van Cauter, T., Moser, M., and Moser, E. (2014). Topography of head direction cells in medial entorhinal cortex. Curr. Biol. *24*, 252–262.

Gogolla, N., LeBlanc, J., Quast, K., Südhof, T., Fagiolini, M., and Hensch, T. (2009). Common circuit defect of excitatory-inhibitory balance in mouse models of autism. J. Neurodev. Disord. *1*, 172–181.

Gonzalez-Burgos, G., and Lewis, D. (2012). NMDA receptor hypofunction, parvalbumin-positive neurons, and cortical gamma oscillations in schizophrenia. Schizophr. Bull. *38*, 950–957.

Groeneboom, N., Yates, S., Puchades, M., and Bjaalie, J. (2020). Nutil: a pre- and post-processing toolbox for histological rodent brain section images. Front. Neuroinform. *14*, 37.

Grünewald, B., Lange, M.D., Werner, C., O'Leary, A., Weishaupt, A., Popp, S., Pearce, D.A., Wiendl, H., Reif, A., Pape, H.C., et al. (2017). Defective synaptic transmission causes disease signs in a mouse model of juvenile neuronal ceroid lipofuscinosis. Elife *6*, e28685.

Hafting, T., Fyhn, M., Molden, S., Moser, M.B., and Moser, E.I. (2005). Microstructure of a spatial map in the entorhinal cortex. Nature *436*, 801–806.

Harris, E., Abel, J., Tejada, L., and Rissman, E. (2016). Calbindin knockout alters sex-specific regulation of behavior and gene expression in amygdala and prefrontal cortex. Endocrinology *157*, 1967–1979.

Hashimoto, T., Volk, D., Eggan, S., Mirnics, K., Pierri, J., Sun, Z., Sampson, A., and Lewis, D. (2003). Gene expression deficits in a subclass of GABA neurons in the prefrontal cortex of subjects with schizophrenia. J. Neurosci. *23*, 6315–6326.

Hedreen, J.C. (1998). Lost caps in histological counting methods. Anat. Rec. *250*, 366–372.

Herculano-Houzel, S., Mota, B., and Lent, R. (2006). Cellular scaling rules for rodent brains. Proc. Natl. Acad. Sci. U S A *103*, 12138–12143.

Hu, H., Gan, J., and Jonas, P. (2014). Fast-spiking, parvalbumin^{+} GABAergic interneurons: from cellular design to microcircuit function. Science *345*, 1255263.

Ibáñez-Sandoval, O., Tecuapetla, F., Unal, B., Shah, F., Koós, T., and Tepper, J.M. (2010). Electrophysiological and morphological characteristics and synaptic connectivity of tyrosine hydroxylase-expressing neurons in adult mouse striatum. J. Neurosci. *30*, 6999–7016.

Jinno, S., and Kosaka, T. (2006). Cellular architecture of the mouse hippocampus: a quantitative aspect of chemically defined GABAergic neurons with stereology. Neurosci. Res. *56*, 229–245.

Kalanithi, P., Zheng, W., Kataoka, Y., DiFiglia, M., Grantz, H., Saper, C., Schwartz, M., Leckman, J., and Vaccarino, F. (2005). Altered parvalbumin-positive neuron distribution in basal ganglia of individuals with Tourette syndrome. Proc. Natl. Acad. Sci. U S A *102*, 13307–13312.

Keller, D., Erö, C., and Markram, H. (2018). Cell densities in the mouse brain: a systematic review. Front. Neuroanat. *12*, 1–21.

Kim, Y., Venkataraju, K.U., Pradhan, K., Mende, C., Taranda, J., Turaga, S.C., Arganda-Carreras, I., Ng, L., Hawrylycz, M.J., Rockland, K.S., et al. (2015). Mapping social behavior-induced brain activation at cellular resolution in the mouse. Cell Rep. *10*, 292–305.

Kim, Y., Yang, G., Pradhan, K., Venkataraju, K., Bota, M., García del Molino, L., Fitzgerald, G., Ram, K., He, M., Levine, J., et al. (2017). Brain-wide maps reveal stereotyped cell-type-based cortical architecture and subcortical sexual dimorphism. Cell *171*, 456–469.

Kjonigsen, L., Lillehaug, S., Bjaalie, J., Witter, M., and Leergaard, T. (2015). Waxholm Space atlas of the rat brain hippocampal region: three-dimensional delineations based on magnetic resonance and diffusion tensor imaging. Neuroimage *108*, 441–449.

Kjonigsen, L.J., Leergaard, T.B., Witter, M.P., and Bjaalie, J.G. (2011). Digital atlas of anatomical subdivisions and boundaries of the rat hippocampal region. Front. Neuroinform. *5*, 2.

Kobro-Flatmoen, A., and Witter, M. (2019). Neuronal chemo-architecture of the entorhinal cortex: a comparative review. Eur. J. Neurosci. *50*, 3627–3662.

Laja, A., Bjerke, I., Leergaard, T., and Witter, M. (2020a). Distribution of parvalbumin-positive interneurons in the normal adult mouse brain. EBRAINS. https://doi.org/10.25493/BXGX-WM4.

Laja, A., Bjerke, I., Leergaard, T., and Witter, M. (2020b). Distribution of parvalbumin-positive interneurons in the normal adult rat brain. EBRAINS. https://doi.org/10.25493/8KCQ-3C7.

Lauber, E., Filice, F., and Schwaller, B. (2016). Prenatal valproate exposure differentially affects parvalbumin-expressing neurons and related circuits in the cortex and striatum of mice. Front. Mol. Neurosci. *9*, 1–16.

Lauber, E., Filice, F., and Schwaller, B. (2018). Dysregulation of parvalbumin expression in the Cntnap2 −/− mouse model of autism spectrum disorder. Front. Mol. Neurosci. *11*, 1–15.

Li, J., Xie, X., Yu, J., Sun, Y., Liao, X., Wang, X., Su, Y., Liu, Y., Schmidt, M., Wang, X., et al. (2017). Suppressed calbindin levels in hippocampal excitatory neurons mediate stress-induced memory loss. Cell Rep. *21*, 897–900.

Lu, E., Llano, D.A., and Sherman, S.M. (2009). Different distributions of calbindin and calretinin immunostaining across the medial and dorsal divisions of the mouse medial geniculate body. Hear. Res. *257*, 16–23.

Madisen, L., Zwingman, T.A., Sunkin, S.M., Oh, S.W., Zariwala, H.A., Gu, H., Ng, L.L., Palmiter, R.D., Hawrylycz, M.J., Jones, A.R., et al. (2010). A robust and high-throughput Cre reporting and characterization system for the whole mouse brain. Nat. Neurosci. *13*, 133–140.

Marder, E., Goeritz, M.L., and Otopalik, A.G. (2015). Robust circuit rhythms in small circuits arise from variable circuit components and mechanisms. Curr. Opin. Neurobiol. *31*, 156–163.

Marín, O. (2012). Interneuron dysfunction in psychiatric disorders. Nat. Rev. Neurosci. *13*, 107–120.

Markram, H., Toledo-Rodriguez, M., Wang, Y., Gupta, A., Silberberg, G., and Wu, C. (2004). Interneurons of the neocortical inhibitory system. Nat. Rev. Neurosci. *5*, 793–807.

Merino-Serrais, P., Tapia-González, S., and DeFelipe, J. (2020). Calbindin immunostaining in the CA1 hippocampal pyramidal cell layer of the human and mouse: a comparative study. J. Chem. Neuroanat. *104*, 101745.

Miao, C., Cao, Q., Moser, M., and Moser, E. (2017). Parvalbumin and somatostatin interneurons control different space-coding networks in the medial entorhinal cortex. Cell *171*, 507–521.

Moreno-Gonzalez, I., Baglietto-Vargas, D., Sanchez-Varo, R., Jimenez, S., Trujillo-Estrada, L., Sanchez-Mejias, E., Del Rio, J.C., Torres, M., Romero-Acebal, M., Ruano, D., et al. (2009). Extracellular amyloid-β and cytotoxic glial activation induce significant entorhinal neuron loss in young PS1M146L/APP751SL mice. J. Alzheimer's Dis. *18*, 755–776.

Murakami, T., Mano, T., Saikawa, S., Horiguchi, S., Shigeta, D., Baba, K., Sekiya, H., Shimizu, Y., Tanaka, K., Kiyonari, H., et al. (2018). A three-dimensional single-cell-resolution whole-brain atlas using CUBIC-X expansion microscopy and tissue clearing. Nat. Neurosci. *21*, 625–637.

Neddens, J., and Buonanno, A. (2009). Selective populations of hippocampal interneurons express ErbB4 and their number and distribution is altered in ErbB4 knockout mice. Hippocampus *20*, 724–744.

Nilssen, E., Jacobsen, B., Fjeld, G., Nair, R., Blankvoort, S., Kentros, C., and Witter, M. (2018). Inhibitory connectivity dominates the fan cell

network in layer II of lateral entorhinal cortex. J. Neurosci. *38*, 9712–9727.

Ohara, S., Gianatti, M., Itou, K., Berndtsson, C.H., Doan, T.P., Kitanishi, T., Mizuseki, K., Iijima, T., Tsutsui, K.-I., and Witter, M.P. (2019). Entorhinal layer II calbindin-expressing neurons originate widespread telencephalic and intrinsic projections. Front. Syst. Neurosci. *13*, 54.

Oorschot, D. (1994). Are you using neuronal densities, synaptic densities or neurochemical densities as your definitive data? There is a better way to go. Prog. Neurobiol. *44*, 233–247.

Papp, E., Leergaard, T., Calabrese, E., Johnson, G., and Bjaalie, J. (2014). Waxholm Space atlas of the Sprague dawley rat brain. Neuroimage *97*, 374–386.

Parrish-Aungst, S., Shipley, M.T., Erdelyi, F., Szabo, G., and Puche, A.C. (2007). Quantitative analysis of neuronal diversity in the mouse olfactory bulb. J. Comp. Neurol. *501*, 825–836.

Pirone, A., Alexander, J., Koenig, J., Cook-Snyder, D., Palnati, M., Wickham, R., Eden, L., Shrestha, N., Reijmers, L., Biederer, T., et al. (2018). Social stimulus causes aberrant activation of the medial prefrontal cortex in a mouse model with autism-like behaviors. Front. Synaptic Neurosci. *10*, 35.

Pitts, M.W., Reeves, M.A., Hashimoto, A.C., Ogawa, A., Kremer, P., Seale, L.A., and Berry, M.J. (2013). Deletion of selenoprotein M leads to obesity without cognitive deficits. J. Biol. Chem. *288*, 26121–26134.

Puchades, M., Csucs, G., Ledergerber, D., Leergaard, T., and Bjaalie, J. (2019). Spatial registration of serial microscopic brain images to three-dimensional reference atlases with the QuickNII tool. PLoS One *14*, e0216796.

Ransome, M.I., and Turnley, A.M. (2005). Analysis of neuronal subpopulations in mice over-expressing suppressor of cytokine signaling-2. Neuroscience *132*, 673–687.

Ray, S., Naumann, R., Burgalossi, A., Tang, Q., Schmidt, H., and Brecht, M. (2014). Grid-layout and theta-modulation of layer 2 pyramidal neurons in medial entorhinal cortex. Science *343*, 891–896.

Rogers, J.H., and Résibois, A. (1992). Calretinin and calbindin-D28k in rat brain: patterns of partial co-localization. Neuroscience *51*, 843–865.

Rudy, B., Fishell, G., Lee, S., and Hjerling-Leffler, J. (2011). Three groups of interneurons account for nearly 100% of neocortical GABAergic neurons. Dev. Neurobiol. *71*, 45–61.

Runyan, C.A., Schummers, J., Van Wart, A., Kuhlman, S.J., Wilson, N.R., Huang, Z.J., and Sur, M. (2010). Response features of parvalbumin-expressing interneurons suggest precise roles for subtypes of inhibition in visual cortex. Neuron *67*, 847–857.

Schmid, J.S., Bernreuther, C., Nikonenko, A.G., Ling, Z., Mies, G., Hossmann, K.A., Jakovcevski, I., and Schachner, M. (2013). Heterozygosity for the mutated X-chromosome-linked L1 cell adhesion molecule gene leads to increased numbers of neurons and enhanced metabolism in the forebrain of female carrier mice. Brain Struct. Funct. *218*, 1375–1390.

Schwaller, B. (2010). Cytosolic Ca2+ buffers. Cold Spring Harb. Perspect. Biol. *2*, a004051.

Schwaller, B. (2020). Cytosolic Ca2+ buffers are inherently Ca2+ signal modulators. Cold Spring Harb. Perspect. Biol. *12*, 1–24.

Silvestri, L., Paciscopi, M., Soda, P., Biamonte, F., Iannello, G., Frasconi, P., and Pavone, F. (2015). Quantitative neuroanatomy of all Purkinje cells with light sheet microscopy and high-throughput image analysis. Front. Neuroanat. *9*, 1–11.

Smith, K.M., Fagel, D.M., Stevens, H.E., Maragnoli, M.E., Rabenstein, R.L., Ohkubo, Y., Picciotto, M.R., Schwartz, M.L., and Vaccarino, F.M. (2008). Deficiency in inhibitory cortical interneurons associates with hyperactivity in fibroblast growth factor receptor 1 mutant mice. Biol. Psychiatry *63*, 953–962.

Song, C.-H., Bernhard, D., Bolarinwa, C., Hess, E.J., Smith, Y., and Jinnah, H.A. (2013). Subtle microstructural changes of the striatum in a DYT1 knock-in mouse model of dystonia. Neurobiol. Dis. *54*, 362–371.

Stensola, H., Stensola, T., Solstad, T., Frøland, K., Moser, M., and Moser, E. (2012). The entorhinal grid map is discretized. Nature *492*, 72–78.

Strange, B.A., Witter, M.P., Lein, E.S., and Moser, E.I. (2014). Functional organization of the hippocampal longitudinal axis. Nat. Rev. Neurosci. *15*, 655–669.

Sun, S., Li, F., Gao, X., Zhu, Y., Chen, J., Zhu, X., Yuan, H., and Gao, D. (2011). Calbindin-D28K inhibits apoptosis in dopaminergic neurons by activation of the PI3-kinase-Akt signaling pathway. Neuroscience *199*, 359–367.

Szabadics, J., Varga, C., Brunner, J., Chen, K., and Soltesz, I. (2010). Granule cells in the CA3 area. J. Neurosci. *30*, 8296–8307.

Tremblay, R., Lee, S., and Rudy, B. (2016). GABAergic interneurons in the neocortex: from cellular properties to circuits. Neuron *91*, 260–292.

Tsao, A., Moser, M.-B., and Moser, E.I. (2013). Traces of experience in the lateral entorhinal cortex. Curr. Biol. *23*, 399–405.

Tsao, A., Sugar, J., Lu, L., Wang, C., Knierim, J., Moser, M., and Moser, E. (2018). Integrating time from experience in the lateral entorhinal cortex. Nature *561*, 57–62.

Wang, Q., Ding, S., Li, Y., Royall, J., Feng, D., Lesnar, P., Graddis, N., Naeemi, M., Facer, B., Ho, A., et al. (2020). The allen mouse brain Common coordinate Framework: a 3D reference atlas. Cell *181*, 1–18.

Wang, X., Tucciarone, J., Jiang, S., Yin, F., Wang, B.S., Wang, D., Jia, Y., Jia, X., Li, Y., Yang, T., et al. (2019). Genetic single neuron anatomy reveals fine granularity of cortical axo-axonic cells. Cell Rep. *26*, 3145–3159.e5.

Yalcin-Cakmakli, G., Rose, S.J., Villalba, R.M., Williams, L., Jinnah, H.A., Hess, E.J., and Smith, Y. (2018). Striatal cholinergic interneurons in a knock-in mouse model of L -DOPA-Responsive dystonia. Front. Syst. Neurosci. *12*, 1–12.

Yates, S., Groeneboom, N., Coello, C., Lichtenthaler, S., Kuhn, P.-H., Demuth, H.-U., Hartlage-Rübsamen, M., Roßner, S., Leergaard, T., Kreshuk, A., et al. (2019). QUINT: workflow for quantification and spatial analysis of features in histological images from rodent brain. Front. Neuroinform. *13*, 1–14.

Yu, J., Gutnisky, D.A., Hires, S.A., and Svoboda, K. (2016). Layer 4 fast-spiking interneurons filter thalamocortical signals during active somatosensation. Nat. Neurosci. *19*, 1647–1657.

Yu, J., Hu, H., Agmon, A., and Svoboda, K. (2019a). Recruitment of GABAergic interneurons in the barrel cortex during active tactile behavior. Neuron *104*, 412–427.

Yu, Q., Liu, Y.Z., Zhu, Y.B., Wang, Y.Y., Li, Q., and Yin, D.M. (2019b). Genetic labeling reveals temporal and spatial expression pattern of D2 dopamine receptor in rat forebrain. Brain Struct. Funct. *224*, 1035–1049.

Zhang, C., Yan, C., Ren, M., Li, A., Quan, T., and Gong, H. (2017). A platform for stereological quantitative analysis of the brain- wide distribution of type-specific neurons. Sci. Rep. *7*, 1–12.

Zilles, K., Bacha-Trams, M., Palomero-Gallagher, N., Amunts, K., and Friederici, A.D. (2015). Common molecular basis of the sentence comprehension network revealed by neurotransmitter receptor fingerprints. Cortex *63*, 79–89.

iScience, Volume *24*

Supplemental Information

Densities and numbers of calbindin and parvalbumin positive neurons across the rat and mouse brain

Ingvild E. Bjerke, Sharon C. Yates, Arthur Laja, Menno P. Witter, Maja A. Puchades, Jan G. Bjaalie, and Trygve B. Leergaard

Supplemental Figure 1. Comparison of manual and QUINT counts of parvalbumin positive profiles across the medial entorhinal cortex. Related to Transparent Methods, "Validity of segmentations".

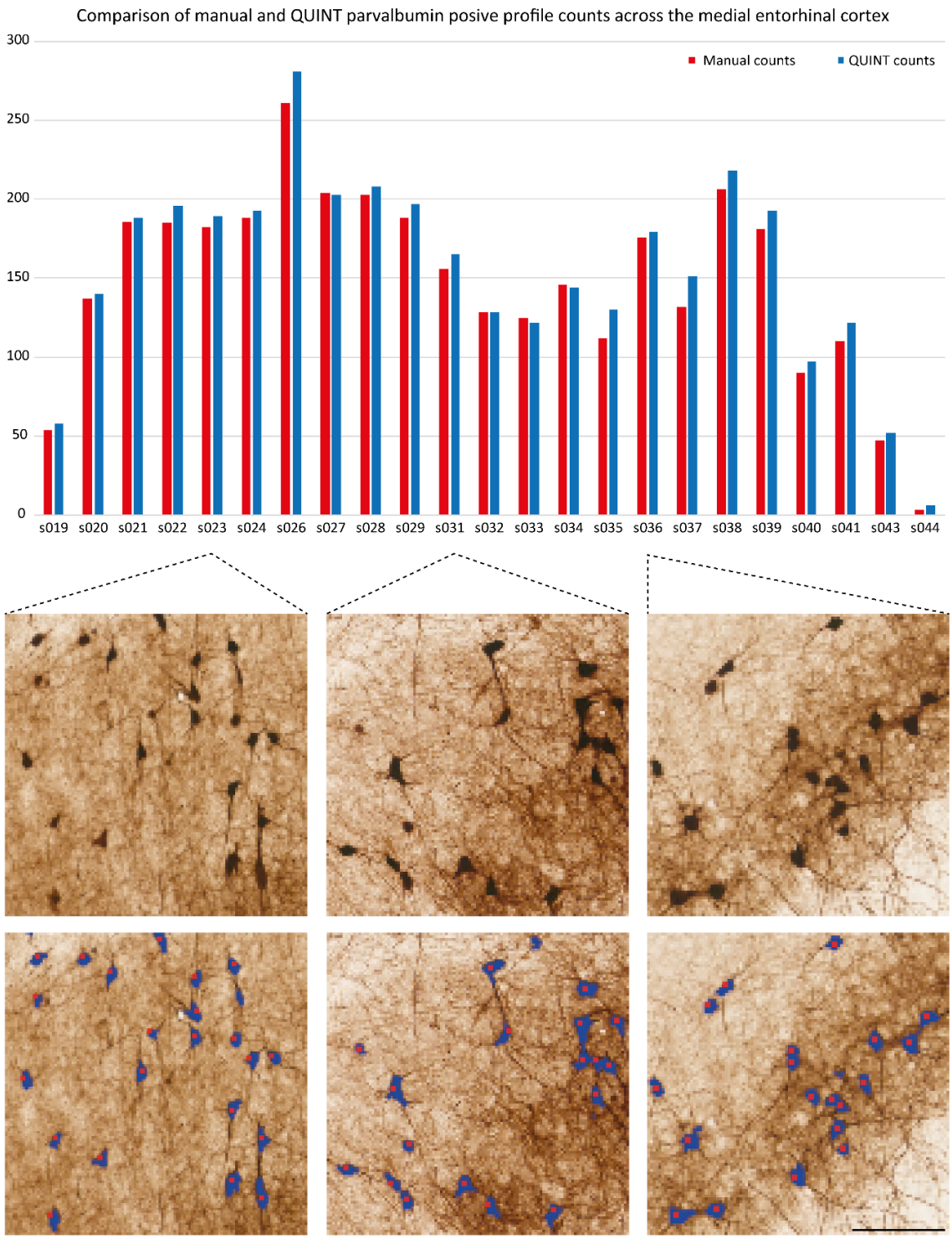

The graph shows manual counts (red bars) and QUINT counts (blue bars) from horizontal sections throughout the medial entorhinal cortex. Bottom row shows example of manual and ilastik segmentations overlayed to the parvalbumin stained material. Scale bar: 100 µm.

Supplemental Figure 2. Reliability of segmentations from one researcher. Related to Transparent Methods, "Reliability of segmentations".

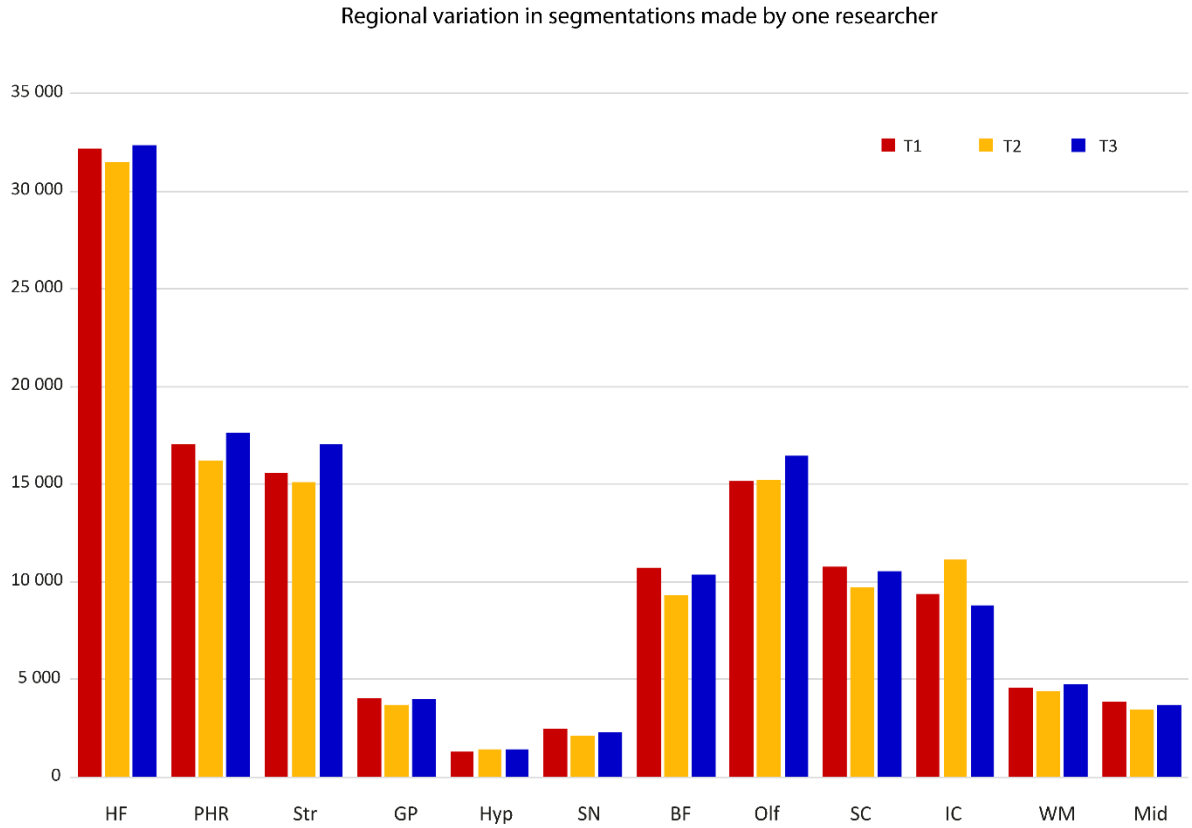

Bar chart showing the results from quantification of segmentations made by one researcher at three different time points (T1-3). Abbreviations: BF, basal forebrain; GP, globus pallidus; HF, hippocampal formation; Hyp, hypothalamus; IC, inferior colliculus; PHR, parahippocampal region; Mid, other midbrain regions Str, striatum; SN, substantia nigra; Olf, olfactory regions; SC, superior colliculus; WM, white matter. A list of which regions of the Waxholm Space rat brain atlas that are grouped in these abbreviations is given in Supplemental Data 1.

Supplemental Figure 3. Reliability of segmentations across researchers. Related to Transparent Methods, "Reliability of segmentations".

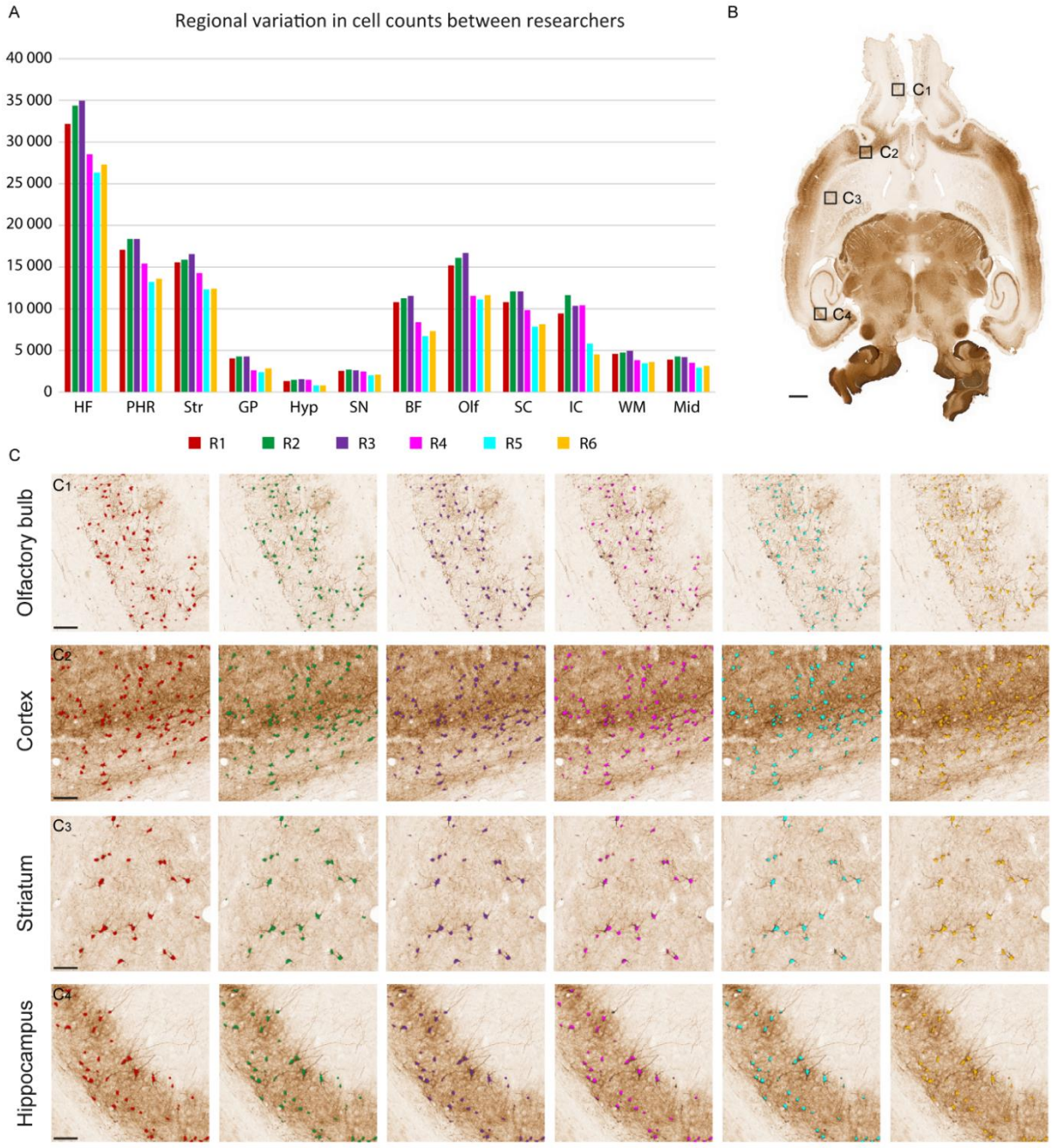

(A) Bar chart showing variations between different researchers segmentation results. One researcher (R1, red bars) performed a segmentation and provided documentation (see, Transparent methods) for replication of the analysis by researchers 2-5. Examples from the segmentations produced by each researcher are shown as overlays on the original images in the lower panel (C1-C4, colour coded in accordance with the bar graph). Scale bars are 1 mm in (B) and 100 µm in C1-C4. Abbreviations: BF, basal forebrain; GP, globus pallidus; HF, hippocampal formation; Hyp, hypothalamus; IC, inferior colliculus; PHR, parahippocampal region; Mid, other midbrain regions Str, striatum; SN, substantia nigra; Olf, olfactory regions; SC, superior colliculus; WM, white matter. A list of which regions of the Waxholm Space rat brain atlas that are grouped in these abbreviations is given in Supplemental Data 1.

Supplemental Figure 4. Examples of images with atlas overlays and segmentation results. Related to Transparent Methods, "Image segmentation".

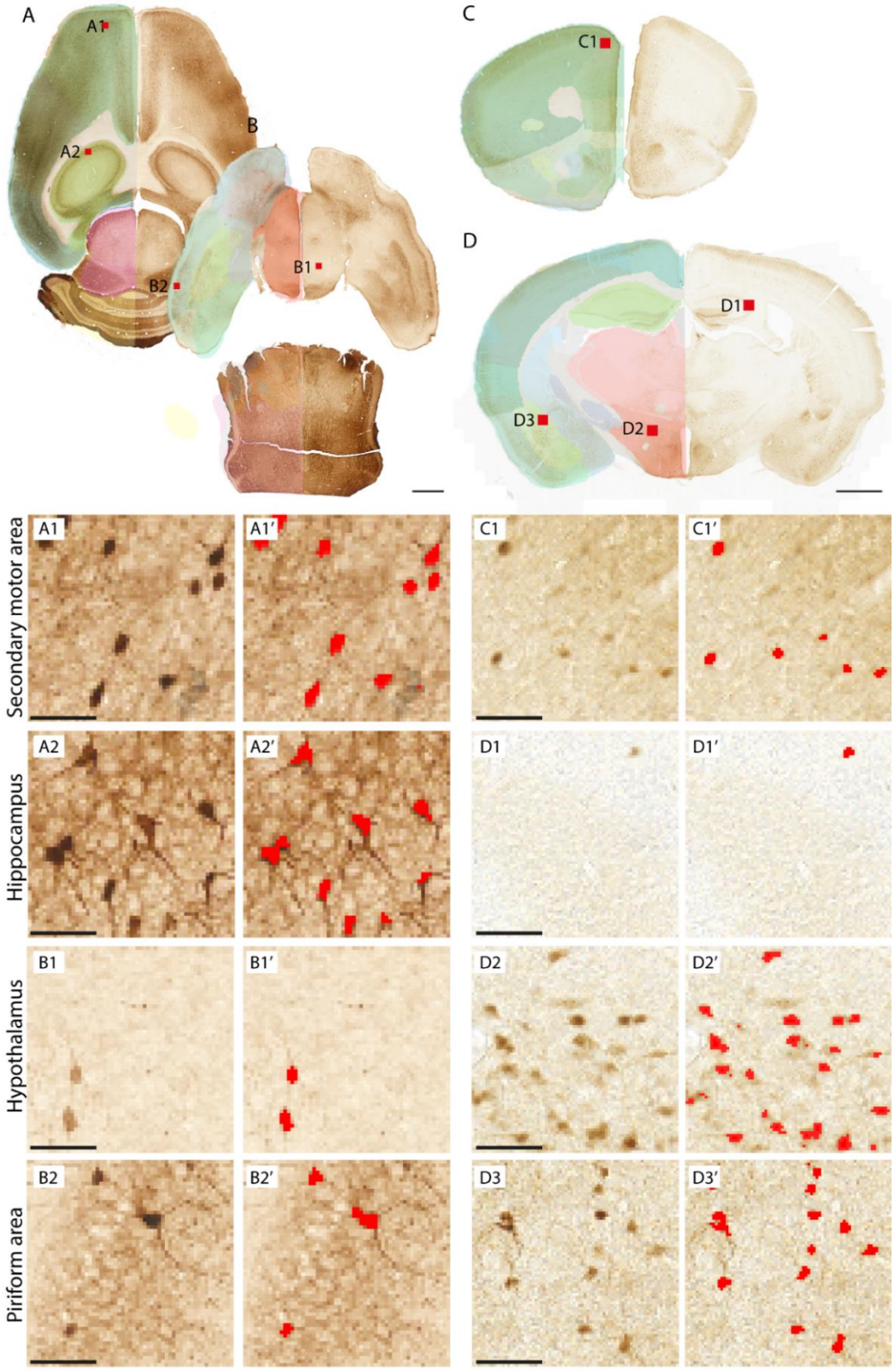

(A,B) show parvalbumin stained sections (from mouse 81265, sections 012 and 041, respectively), and (C,D) show calbindin stained sections (from mouse 6, sections 097 and 181, respectively). Atlas overlays are superimposed on one hemisphere. (A1-2, B1-2, C1, and D1-3) are enlarged images from selected regions as indicated in (A-D), showing regions secondary motor area (A1, C1), hippocampus (A2, D1), hypothalamus (A3, D2), and piriform area (A4, D3). Panels (A1'-2', B1'-2', C1' and D1'-3') show ilastik segmentations used for QUINT counts of labelled cells. Some lightly stained calbindin neurons (e.g. in hypothalamus) were not extracted by our classifier. Images are shown at the reduced resolution used for this analysis, high-resolution images are available from the shared datasets. Scale bars: upper panels, 1 mm; lower panels, 50 µm.

Supplemental table 1: List of calbindin and parvalbumin numbers and densities in the mouse brain (related to Figure 2)

Volume: region volume in mm³ **Number:** bilateral total number estimate **Density:** estimated number per mm³		Volume	Parvalbumin		Calbindin	
			Number	Density	Number	Density
Isocortex (ISO)						
FRP	Frontal pole, cerebral cortex	0.97	1 053 ± 148	1 081 ± 152	518 ± 214	532 ± 219
MOp	Primary motor area	12.19	15 446 ± 2 596	1 267 ± 213	10 727 ± 2 049	880 ± 168
MOs	Secondary motor area	13.10	16 519 ± 3 579	1 261 ± 273	10 254 ± 1 558	783 ± 119
Somatosensory areas (SS)						
SSp-n	Primary somatosensory area, nose	3.02	4 702 ± 204	1 557 ± 68	2 795 ± 513	926 ± 170
SSP-bfd	Primary somatosensory area, barrel field	6.29	10 518 ± 1 048	1 673 ± 167	6 164 ± 10 05	980 ± 160
SSP-ll	Primary somatosensory area, lower limb	2.35	4 272 ± 383	1 816 ± 163	3 711 ± 609	1 578 ± 259
SSP-m	Primary somatosensory area, mouth	6.21	7 289 ± 685	1 174 ± 110	4 854 ± 748	782 ± 120
SSP-ul	Primary somatosensory area, upper limb	3.77	6 659 ± 1 207	1 766 ± 320	4 566 ± 819	1 211 ± 217
SSP-tr	Primary somatosensory area, trunk	1.40	2 778 ± 425	1 982 ± 303	2 218 ± 253	1 582 ± 181
SSP-un	Primary somatosensory area, unassigned	1.26	2 478 ± 274	1 963 ± 217	1 537 ± 277	1 218 ± 220
SSs	Supplemental somatosensory area	9.01	13 299 ± 670	1 475 ± 74	10 155 ± 1 908	1 126 ± 212
Gustatory and visceral areas						
GU	Gustatory areas	1.77	2 116 ± 392	1 197 ± 222	3 343 ± 423	1 890 ± 239
VISC	Visceral areas	2.35	2 789 ± 287	1 187 ± 122	3 874 ± 521	1 649 ± 222
Auditory areas (AUD)						
AUDd	Dorsal auditory area	1.21	2 217 ± 302	1 825 ± 249	987 ± 133	813 ± 109
AUDp	Primary auditory area	2.15	4 173 ± 744	1 942 ± 346	1 920 ± 287	893 ± 133
AUDpo	Posterior auditory area	0.61	855 ± 163	1 397 ± 267	934 ± 136	1 526 ± 222
AUDv	Ventral auditory area	1.82	3 311 ± 607	1 821 ± 334	2 087 ± 271	1 148 ± 149
Visual areas (VIS)						
VISal	Anterolateral visual area	0.76	1 291 ± 183	1 703 ± 241	990 ± 104	1 306 ± 137
VISam	Anteromedial visual area	0.79	1 883 ± 393	2 376 ± 496	933 ± 104	1 178 ± 204
VISl	Lateral visual area	1.23	1978 ± 413	1 614 ± 337	1 772 ± 308	1 446 ± 251
VISp	Primary visual area	7.07	13 120 ± 2 514	1 855 ± 355	10 063 ± 1 333	1 423 ± 288
VISpl	Posterolateral visual area	0.79	1 190 ± 300	1 498 ± 378	1 150 ± 292	1 447 ± 367
VISpm	Posteromedial visual area	1.04	2 350 ± 381	2 241 ± 364	1 764 ± 285	1 682 ± 272
VISli	Laterointermediate area	0.49	688 ± 84	1 398 ± 170	791 ± 121	1 608 ± 246
VISpor	Postrhinal area	1.29	1 976 ± 458	1 541 ± 357	2 131 ± 165	1 662 ± 129
Anterior cingulate areas (ACA)						
ACAd	Anterior cingulate area, dorsal part	3.13	5 890 ± 1 570	1 881 ± 501	3 702 ± 570	1 182 ± 182
ACAv	Anterior cingulate area, ventral part	2.41	4 558 ± 706	1 893 ± 293	4 428 ± 505	1 838 ± 210
Prefrontal areas (PFA)						
PL	Prelimbic area	2.41	3 116 ± 551	1 293 ± 229	3 713 ± 322	1 541 ± 133
ILA	Infralimbic area	0.84	925 ± 190	1 095 ± 224	2 960 ± 211	3 506 ± 249
ORB	Orbital area	5.90	9 678 ± 1 632	1 640 ± 277	8 547 ± 1 376	1 448 ± 233
AGA	Agranular insular area	7.89	8 052 ± 1 290	1 020 ± 163	15 332 ± 1 448	1 942 ± 183
Retrosplenial areas (RSP)						
RSPagl	Retrosplenial area, lateral agranular part	2.35	3 822 ± 723	1 621 ± 307	3 563 ± 515	1 512 ± 218
RSPd	Retrosplenial area, dorsal part	3.80	5 142 ± 800	1 353 ± 211	3 052 ± 494	803 ± 130
RSPv	Retrosplenial area, ventral part	4.35	7 727 ± 398	1 777 ± 92	1 331 ± 239	306 ± 55

Other isocortical areas (ISOo)						
PTLp	Posterior parietal association areas	2.46	4 121 ± 704	1 677 ± 287	2 439 ± 94	993 ± 38
TEa	Temporal association areas	3.10	4 494 ± 957	1 449 ± 309	4 645 ± 425	1 497 ± 137
PERI	Perirhinal area	0.79	526 ± 130	666 ± 165	1 169 ± 169	1 481 ± 214
ECT	Ectorhinal area	1.71	1 823 ± 298	1 065 ± 174	2 795 ± 277	1 632 ± 162
Olfactory areas (OLF)						
MOB	Main olfactory bulb	21.49	10 714 ± 4 632	499 ± 216	18 784 ± 1 355	874 ± 63
AOB	Accessory olfactory bulb	0.65	65 ± 31	100 ± 48	107 ± 31	164 ± 48
AON	Accessory olfactory nucleus	4.87	2 093 ± 704	430 ± 145	9 332 ± 987	1 916 ± 203
TT	Taenia tecta	1.44	672 ± 235	466 ± 163	1 574 ± 144	1 092 ± 100
DP	Dorsal peduncular nucleus	0.50	754 ± 199	1 493 ± 394	1 677 ± 79	3 324 ± 156
PIR	Piriform area	11.57	6 108 ± 899	528 ± 78	17 379 ± 865	1 502 ± 75
NLOT	Nucleus of the lateral olfactory tract	0.32	113 ± 39	353 ± 122	563 ± 132	1 763 ± 414
COA	Cortical amygdalar area	3.27	1 392 ± 281	426 ± 86	7 589 ± 843	2 324 ± 258
PAA	Piriform-amygdalar area	1.19	237 ± 138	199 ± 116	1 660 ± 199	1 393 ± 167
TR	Postpiriform transition area	1.40	795 ± 178	566 ± 127	3 559 ± 417	2 534 ± 297
Hippocampal formation (HPF)						
Hippocampal region (HR)						
CA1	Field CA1	10.19	6 631 ± 1 221	651 ± 120	5 893 ± 1 257	578 ± 123
CA2	Field CA2	0.48	391 ± 61	823 ± 127	84 ± 19	177 ± 40
CA3	Field CA3	6.26	3 835 ± 950	612 ± 152	1 638 ± 110	262 ± 17
DG	Dentate gyrus	6.60	1 173 ± 372	178 ± 56	5 778 ± 896	876 ± 136
FC	Fasciola cinerea	0.06	61 ± 19	996 ± 304	1 ± 1	16 ± 16
IG	Induseum griseum	0.12	45 ± 15	355 ± 115	23 ± 7	183 ± 54
Retrohippocampal region (RHP)						
ENTl	Entorhinal area, lateral part	6.38	3 869 ± 478	607 ± 75	10 580 ± 1 257	1 659 ± 197
ENTm	Entorhinal area, medial part	5.02	8 384 ± 940	1 671 ± 187	4 962 ± 586	989 ± 117
PAR	Parasubiculum	0.93	2 439 ± 251	2 614 ± 269	658 ± 83	706 ± 89
POST	Postsubiculum	1.08	2 264 ± 397	2 088 ± 366	528 ± 112	487 ± 104
PRE	Presubiculum	0.92	2 314 ± 366	2 525 ± 400	479 ± 134	523 ± 146
SUB	Subiculum	2.10	4 347 ± 355	2 072 ± 169	909 ± 221	433 ± 106
ProS	Prosubiculum	1.33	1 550 ± 205	1 167 ± 155	924 ± 141	696 ± 106
HATA	Hippocampo-amygdalar transition area	0.42	441 ± 125	1 047 ± 296	1 061 ± 128	2 519 ± 303
APr	Area prostriata	0.32	432 ± 30	1 324 ± 91	279 ± 64	853 ± 263
Cortical subplate (CTXsp)						
CLA	Claustrum	0.55	397 ± 45	721 ± 82	859 ± 64	1 559 ± 116
EP	Endopiriform nucleus	2.79	1 330 ± 230	476 ± 82	6 186 ± 477	2 215 ± 171
LA	Lateral amygdalar nucleus	0.84	351 ± 65	418 ± 77	829 ± 130	986 ± 154
BLA	Basolateral amygdalar nucleus	1.90	1 151 ± 308	606 ± 162	4 486 ± 631	2 361 ± 332
BMA	Basomedial amygdalar nucleus	1.49	841 ± 245	567 ± 165	4 109 ± 681	2 766 ± 458
PA	Posterior amygdalar nucleus	0.97	1 304 ± 482	1 349 ± 499	5 554 ± 569	5 745 ± 589
Cerebral nuclei (CNU)						
Striatum (STR)						
CP	Caudoputamen	26.01	15 015 ± 519	577 ± 20	48 064 ± 7 665	1 847 ± 295
STRv	Striatum ventral region	4.83	1 578 ± 206	327 ± 43	10 027 ± 1 326	2 076 ± 275
OT	Olfactory tubercle	3.82	1 327 ± 283	347 ± 74	1 597 ± 182	418 ± 48
LSX	Lateral septal complex	3.56	444 ± 119	125 ± 33	11 005 ± 982	3 088 ± 276
sAMY	Striatum-like amygdalar nuclei	4.05	871 ± 200	215 ± 49	10 291 ± 1 188	2 540 ± 293
Pallidum (PAL)						
GPe	Globus pallidus, external segment	1.56	337 ± 220	216 ± 140	350 ± 38	223 ± 24
GPi	Globus pallidus, internal segment	0.42	108 ± 49	254 ± 115	24 ± 7	57 ± 16
PALv	Pallidum, ventral region	3.39	1 496 ± 298	441 ± 88	3 196 ± 462	942 ± 136
PALm	Pallidum, medial region	1.51	1 060 ± 359	701 ± 238	3 766 ± 712	2 492 ± 471
BST	Bed nuclei of the stria terminalis	1.34	216 ± 58	161 ± 43	5 832 ± 1 067	4 349 ± 796
Thalamus (TH)						
VENT	Ventral group of the dorsal thalamus	4.86	1 267 ± 315	261 ± 65	5 078 ± 1 282	1 045 ± 264
SPF	Subparafascicular nucleus	0.20	7 ± 3	32 ± 15	507 ± 97	2 474 ± 474
SPA	Subparafascicular area	0.13	4 ± 2	28 ± 14	658 ± 202	4 964 ± 1 526
PP	Peripeduncular area	0.06	6 ± 4	96 ± 68	389 ± 91	6 359 ± 1 482

GENd	Geniculate group, dorsal thalamus	1.42	58 ± 26	41 ± 18	893 ± 241	628 ± 170
LAT	Lateral group of the dorsal thalamus	3.08	323 ± 98	105 ± 32	3 540 ± 860	1 151 ± 279
ATN	Anterior group of the dorsal thalamus	2.16	304 ± 70	141 ± 33	1 084 ± 314	502 ± 146
MED	Medial group of the dorsal thalamus	2.08	247 ± 33	123 ± 16	5 844 ± 1 328	2 897 ± 658
MTN	Midline group of the dorsal thalamus	1.19	121 ± 44	102 ± 37	5 438 ± 976	4 585 ± 823
ILM	Intralaminar nuclei of the dorsal thalamus	1.60	78 ± 29	49 ± 18	3 880 ± 932	2 424 ± 582
RT	Reticular nucleus of the thalamus	-	-	-	416 ± 70	287 ± 48
GENv	Geniculate group, ventral thalamus	0.52	282 ± 118	539 ± 225	405 ± 71	773 ± 136
EPI	Epithalamus	0.66	124 ± 58	186 ± 87	1 920 ± 285	2 888 ± 429
Hypothalamus (HY)						
PVZ	Periventricular zone	0.78	62 ± 28	79 ± 36	2 046 ± 240	2 614 ± 307
PVR	Periventricular region	2.04	580 ± 126	283 ± 61	5 859 ± 815	2 864 ± 398
AHN	Anterior hypothalamic nucleus	0.71	274 ± 103	385 ± 145	3 881 ± 592	5 462 ± 833
MBO	Mammillary body	1.02	902 ± 175	888 ± 172	3 779 ± 578	3 720 ± 569
MPN	Medial preoptic nucleus	0.41	47 ± 16	115 ± 40	3 253 ± 396	8 003 ± 975
PM	Premammillary nuclei	0.33	113 ± 37	344 ± 113	721 ±234	2 202 ± 716
PVH	Paraventricular hypothalamic nucleus, descending division	0.13	13 ± 8	101 ± 64	542 ± 29	4 150 ± 219
VMH	Ventromedial hypothalamic nucleus	0.55	85 ± 19	154 ± 35	3 460 ± 404	6 298 ± 736
PH	Posterior hypothalamic nucleus	0.71	65 ± 18	92 ± 26	893 ± 255	1 263 ± 360
LZ	Hypothalamic lateral zone	5.69	2 017 ± 620	355 ± 109	8 049 ± 1 250	1 416 ± 220
ME	Median eminence	0.09	0 ± 0	0 ± 0	6 ± 5	74 ± 60
Midbrain (MB)						
Midbrain, sensory related (MBsen)						
SCs	Superior colliculus, sensory related	2.16	3 813 ± 554	1 768 ± 257	7 213 ± 928	3 345 ± 430
IC	Inferior colliculus	4.44	6 011 ± 1 424	1 352 ± 320	450 ± 65	101 ± 15
NB	Nucleus of the brachium of the inferior colliculus	0.09	67 ± 19	766 ± 214	32 ± 11	359 ± 129
SAG	Nucleus sagulum	0.10	66 ± 38	671 ± 391	15 ± 4	148 ± 43
PBG	Parabigeminal nucleus	0.04	26 ± 11	572 ± 254	3 ± 2	45 ± 45
MEV	Midbrain trigeminal nucleus	0.01	2 ± 1	231 ± 148	15 ± 3	1 585 ± 289
SCO	Subcommissural organ	0.01	8 ± 5	556 ± 313	3 ± 2	208 ± 138
SN	Substantia nigra	1.74	342 ± 138	196 ± 79	132 ± 39	76 ± 23
Midbrain, motor related (MBmot)						
VTA	Ventral tegmental area	0.43	146 ± 60	341 ± 140	1 860 ± 392	4 339 ± 914
PN	Paranigral nucleus	0.02	2 ± 1	101 ± 64	64 ± 13	2 951 ± 620
MRN	Midbrain reticular nucleus	5.28	2 449 ± 733	464 ± 139	901 ± 241	171 ± 46
SCm	Superior colliculus, motor related	5.65	3 981 ± 1 345	704 ± 238	2 716 ± 836	480 ± 148
PAG	Periaqueductal grey	4.69	833 ± 352	178 ± 75	5 962 ± 1 231	1 270 ± 262
PRT	Pretectal region	2.08	1 380 ± 434	663 ± 209	578 ± 119	278 ± 57
MBm-o	Midbrain, motor related, other	1.60	822 ± 152	517 ± 96	296 ± 55	186 ± 35
Midbrain, behavioral state related (MBsta)						
PPN	Pedunculopontine nucleus	0.89	332 ± 98	372 ± 110	461 ± 133	516 ± 149
RAmb	Midbrain raphe nuclei	0.73	345 ± 127	471 ± 173	1 373 ± 272	1 872 ± 371
Pons (PE)						
P-sen	Pons, sensory related	3.85	5 099 ± 483	1 324 ± 126	3 128 ± 691	812 ± 179
P-mot	Pons, motor related	8.16	2 478 ± 1 092	304 ± 30	985 ± 156	121 ± 19
P-sat	Pons, behavioral state related	1.10	1 015 ± 285	923 ± 259	871 ± 248	792 ± 226
Medulla (MY)						
MY-ua	Medulla, unassigned	5.32	2 545 ± 483	478 ± 91	1 032 ± 409	194 ± 77
MY-sen	Medulla, sensory related	7.83	13 232 ± 1 092	1 690 ± 140	4 821 ± 2 155	616 ± 275
MY-mot	Medulla, motor related	19.75	11 369 ± 1 141	576 ± 58	3 493 ± 1 090	177 ± 55
MY-sat	Medulla, behavioral state related	0.22	55 ± 14	245 ± 63	30 ± 10	134 ± 46

Supplemental Table 2: List of mouse parvalbumin literature sources (related to Figure 5)

Mouse parvalbumin neuron densities								
Source	**PMID**	**Strain**	**Brain region**	**# of animals**	**Counting method**	**Section thickness**	**Density (mm^3)**	**Antibody**
Grünewald et al., 2017	29135436	129/Sv	Amygdala (whole region)	14	Direct count	30	2 649	RRID: AB_2631173
Fasulo et al., 2017	28232789	Other	Basolateral amygdala	4	Stereology	40	1 400	No info
Jinno and Kosaka, 2006	16930755	C57BL/6J	CA1	4	Stereology	50	1 405	Kägi et al. (1987)
Neddens and Buonanno, 2009	19655320	C57BL/6	CA1	4	Direct count	50	1 158	rabbit polyclonal anti pv, Swant
Pitts et al., 2013	23880772	C57BL/6J	CA1 of dorsal hippocampus	6	Stereology	40	1 480	RRID:AB_10000344
Pitts et al., 2013	23880772	C57BL/6J	CA2/3 of dorsal hippocampus	6	Stereology	40	2 171	RRID:AB_10000344
Jinno and Kosaka, 2006	16930755	C57BL/6J	CA3	4	Stereology	50	1 535	Kägi et al. (1987)
Neddens and Buonanno, 2009	19655320	C57BL/6	CA3	4	Direct count	50	1 127	rabbit polyclonal anti pv, Swant
Grünewald et al., 2017	29135436	129/Sv	CA3	14	Stereology	30	5 796	RRID: AB_2631173
Filice et al., 2016*	26819149	C57BL/6J	Caudoputamen	5	Stereology		897	RRID:AB_10000344
Lauber et al., 2018*	30116174	C57BL/6J	Caudoputamen	6	Stereology		819	RRID:AB_10000344
Lauber et al., 2016*	28066177	C57BL/6J	Caudoputamen	5	Stereology		817	RRID:AB_10000344
Andsberg et al., 2001*	11358448	C57BL/6J	Caudoputamen	7	Stereology	40	864	polyclonal rabbit anti pv
Smith et al., 2008	17988653	Other	Caudoputamen	3	Stereology	50	3 522	No info
Yalcin-Cakmakli et al., 2018*	29997483	C57BL/6J x DBA/2J	Caudoputamen	3	Stereology	30	953	RRID:AB_2631173
Song et al., 2013*	23336980	C57BL/6J	Caudoputamen	12	Stereology	40	612	No info
Filice et al., 2016*	26819149	C57BL/6J	Caudoputamen	5	Stereology		714	RRID:AB_10000344
Ransome and Turnley, 2005	15837129	C57BL/6	Caudoputamen	3	Stereology	30	1 060	mouse anti-parvalbumin, Chemicon
Förster, 2008	**	C57BL/6J	Caudoputamen	6	Stereology	25	1 430	PARV-19, Sigma
Fasulo et al., 2017	28232789	Other	Dentate gyrus	4	Stereology	40	400	No info
Fasulo et al., 2017	28232789	Other	Dentate gyrus	4	Stereology	40	1 200	No info
Fasulo et al., 2017	28232789	Other	Dentate gyrus	4	Stereology	40	1 100	No info
Jinno and Kosaka, 2006	16930755	C57BL/6J	Dentate gyrus	4	Stereology	50	650	Kägi et al. (1987)
Neddens and Buonanno, 2009	19655320	C57BL/6	Dentate gyrus	4	Direct count	50	745	rabbit polyclonal anti pv, Swant
Pitts et al., 2013	23880772	C57BL/6J	Dentate gyrus of dorsal hippocampus	6	Stereology	40	493	RRID:AB_10000344
Smith et al., 2008*	17988653	Other	Globus pallidus	3	Stereology	50	40 194	No info
Pitts et al., 2013	23880772	C57BL/6J	Inferior colliculus	6	Stereology	40	4 836	RRID:AB_10000344
Moreno-Gonzalez et al., 2009	19661615	C57BL/6	Lateral entorhinal area	5	Stereology	40	4 300	rabbit polyclonal anti pv, Swant
Parrish-Aungst et al., 2007	17311323	C57BL/6J	Main olfactory bulb	4	Stereology	25	2 324	RRID:AB_10000343
Pirone et al., 2018	30369876	Other	Medial prefrontal cortex (infralimbic)	3	Direct count	20	2 052	RRID: AB_2631173
Pirone et al., 2018	30369876	Other	Medial prefrontal cortex (prelimbic)	3	Direct count	20	3 167	RRID: AB_2631173
Pitts et al., 2013	23880772	C57BL/6J	Medial septum	6	Stereology	40	1 678	RRID:AB_10000344
Smith et al., 2008*	17988653	Other	Nucleus accumbens	3	Stereology	50	2 557	No info

Source	PMID	Strain	Brain region	# of animals	Counting method	Section thickness	Density (mm^3)	Antibody
Sanchez-Mejias et al., 2020	31491047	C57BL/6J	Perirhinal area 35	3	Stereology	40	10 765	No info
Sanchez-Mejias et al., 2020	31491047	C57BL/6J	Perirhinal area 36	3	Stereology	40	10 974	No info
Ransome and Turnley, 2005	15837129	C57BL/6	Somatosensory cortex	3	Stereology	30	4 580	mouse anti-parvalbumin, Chemicon
Pitts et al., 2013	23880772	C57BL/6J	Somatosensory cortex	6	Stereology	40	5 329	RRID:AB_10000344
Neddens and Buonanno, 2009	19655320	C57BL/6	Subiculum	4	Direct count	50	2 048	rabbit polyclonal anti pv, Swant
Trujillo-Estrada et al., 2014	24927710	C57BL/6	Subiculum	5	Stereology	40	10 721	rabbit polyclonal anti pv, Swant

* These densities were obtained by dividing total number estimates reported in sources by the volume of the region (as defined by the Allen Mouse brain Common Coordinate Framework, version 3, 2017 edition; see main text for details).
** Thesis, no PMID available. Available from: http://citeseerx.ist.psu.edu/viewdoc/download?doi=10.1.1.427.6474&rep=rep1&type=pdf

Supplemental Table 3: List of mouse calbindin literature sources (related to Figure 2)

Mouse calbindin neuron densities								
Source	PMID	Strain	Brain region	# of animals	Counting method	Section thickness	Density per mm^3	Antibody
Grünewald et al., 2017	29135436	129/Sv	Amygdala (whole region)	12	Direct count	30	5 005	RRID: AB_10000340
Grünewald et al., 2017	29135436	129/Sv	CA3	14	Stereology	30	945	RRID: AB_10000340
Jinno and Kosaka, 2006	16930755	C57BL/6J	CA1	4	Stereology	50	1 555	Pinol et al. (1990)
Jinno and Kosaka, 2006	16930755	C57BL/6J	CA3	4	Stereology	50	1 590	Pinol et al. (1990)
Jinno and Kosaka, 2006	16930755	C57BL/6J	DG	4	Stereology	50	210	Pinol et al. (1990)
Parrish-Aungst et al., 2007	17311323	C57BL/6J	Main olfactory bulb	4	Stereology	25	10 916	RRID:AB_2721225

Supplemental Table 4: List of rat parvalbumin literature sources (related to Figure 2)

Rat parvalbumin neuron densities								
Source		**Strain**	**Brain region**	**# of animals**	**Counting method**	**Section thickness**	**Density (mm^3)**	**Antibody**
Wang et al., 2008	18059437	Sprague-Dawley	CA1		Direct count	50	1 600	RRID:AB_477329
Bezaire and Soltesz, 2013	23674373	-	CA1	-	See legend*	-	-	-
Aika et al., 1994	7925807	Wistar	CA1, dorsal	5	Stereology	0,5	1 100	Polyclonal rabbit anti PV antibody
Wang et al., 2008	18059437	Sprague-Dawley	Caudoputamen		Direct count	50	846	RRID:AB_477329
Kaalund et al., 2013	23083323	Lister Hooded	Dentate gyrus		Stereology	60	2 128	No info
Megahed et al., 2015	25620912	Sprague-Dawley	Dentate gyrus	6	Stereology	30	2 125	No info
Shiraki et al., 2016	27553673	Sprague-Dawley	Dentate gyrus hilus	10	Direct count	3	1 461	PARV-19 Millipore
Kaalund et al., 2013	23083323	Lister Hooded	Hippocampus CA		Stereology	60	2 994	No info
Megahed et al., 2015	25620912	Sprague-Dawley	Hippocampus CA	6	Stereology	30	3 064	No info
Barinka et al., 2012	22221733	Wistar	Perirhinal area 35	6	Stereology		3 805	Monoclonal mouse anti PV
Barinka et al., 2012	22221733	Wistar	Perirhinal area 36	6	Stereology		4 336	Monoclonal mouse anti PV

***** Bezaire & Soltesz (2013) used a combination of literature derived data and calculations to arrive at an estimate of parvalbumin neurons in the rat CA1 (10010 parvalbumin positive neurons unilaterally). Our estimate is 9 198 parvalbumin positive neurons unilaterally in rat CA1.

Transparent methods

EXPERIMENTAL MODEL AND SUBJECT DETAILS

Experimental procedures involving animals were approved by the Norwegian Food Safety Authority and carried out in accordance with the European Union and International legislation for the use of animal subjects. Four adult (6 months old) male PVCre X Rosa26eYFP mice (RRID:IMSR_JAX:008069 and RRID:IMSR_JAX:007903, respectively, crossed locally) and four adult female Sprague-Dawley rats (3 months old, Charles River, Sulzfeld/Kisslegg, Germany) housed at the Kavli Institute, Norwegian Institute of Science and Technology (NTNU), Norway were used for parvalbumin immunohistochemistry. Six adult C57Bl6/J mice (four females and two males, four months old, females from Janvier Labs and males from Taconic), housed at the Institute for Basic Medical Sciences, University of Oslo, Norway, were used for calbindin immunohistochemistry. Animals were housed according to the recommendations by FELASA under pathogen free conditions, with the exception of the presence of Entamoeba muris detected by PCR in fecal samples for the rats. Up to two rats and five mice of the same sex were group-housed in transparent, semi-enriched cages with 12:12 reversed day / night cycles and ad libitum access to food and water.

DATA ACQUISITION

Immunohistochemistry

For parvalbumin immunohistochemistry, animals were deeply anesthetised with sodium pentobarbital (50 mg/kg body weight) and transcardially perfused with Ringer solution containing 4 % paraformaldehyde (PFA). Brains were postfixed in PFA for approximately 24 hours and cryoprotected in a solution of 2 % DMSO and 20 % glycerol in phosphate buffer (PB). Horizontal sections were cut at 30 µm (mouse brains) or 40 µm (rat brains) on a freezing microtome. For calbindin immunohistochemistry, mice were anesthetized with isofluorane, given an overdose of Zoletil mixture, and transcardially perfused with NAPI followed by 4 % PFA. The brains were postfixed overnight in the same fixative, and transferred to 0.4 % PFA for storage. Prior to cutting, the brains were cryoprotected by immersion in 10, 20 and 30 % sucrose until they sank. The right hemisphere was marked by making shallow cut in the cortical surface. Brains were coronally divided at the level of the dorsal hippocampus before coronal sections of 40 µm were cut using a freezing microtome. For all experiments, free-floating sections were used for immunohistochemistry according to the avidin-biotin peroxidase method, using 3,3'-diaminobenzidine (DAB) as the chromogen (every fourth for parvalbumin immunohistochemistry, and every sixth for calbindin). All subsequent steps were performed at room temperature, unless otherwise specified.

Parvalbumin immunohistochemistry. Sections were rinsed with PB before blocking endogenous peroxidase activity by incubation in a solution of 3 % H_2O_2 and 10 % methanol in PB. Sections were rinsed again with PB, but subsequent washes were done using Tris buffered saline with 0.5% triton (TBS-TX). The sections were pre-incubated for 1 hour in 5 % normal goat serum in TBS-TX before overnight incubation at 4°C with the primary antibodies (diluted 1:4000 in TBS-TX). A monoclonal mouse anti-parvalbumin antibody (RRID:AB_477329) was used for the rat brain sections, and a monoclonal rabbit anti parvalbumin (RRID:AB_2631173) for the mouse brain sections. After rinsing, sections were incubated overnight at 4°C with polyclonal, biotinylated secondary antibodies: a goat anti mouse (RRID:AB_258604) antibody for the rat brain sections and a goat anti rabbit (RRID:AB_258649) antibody for the mouse brain sections. Sections were rinsed and then incubated for 1.5 hour with the VectaStain ABC HRP kit, according to manufacturer's instructions. After rinsing again with TBS-TX, the sections were rinsed twice with Tris-HCl before incubation with the DAB solution. The solution was made by adding a 10 mg DAB tablet to 20 mL Tris-HCl, and the tablet was dissolved by placing the solution on a heated stirrer for 2 hours. Afterwards, H_20_2 was added to the solution, which was then placed in the freezer for 20 minutes to slow down the reaction with the sections. The sections were incubated with the DAB solution for approximately 3 minutes and then rinsed with Tris-HCl. The sections were mounted on Superfrost microscope slides with Tris-HCl, and then dried and coverslipped using Entellan (Merck Millipore, Darmstadt, Germany).

Calbindin immunohistochemistry. Sections were rinsed with PBS three times. Endogeneous peroxidase activity was blocked by incubating sections with 3% H_2O_2 for five minutes. After three brief rinses in PBS, sections were incubated in blocking solution (3% normal donkey serum, 1% BSA and 0.1% triton X in PBS) for 1 hour. Sections were incubated in the primary antibody (monoclonal mouse anti calbindin, Swant 300, RRID:AB_10000347, lot no. 07F) overnight at 4°C. The antibody is specific to calbindin-D28k and does not bind to calretinin or other known calcium bindin proteins (manufacturer's description). Control sections processed without the primary antibody did not show specific labelling, and are shared together with the data sets. The next day, sections were washed in PBS before incubation with the secondary antibody (sheep anti mouse, GE Healthcare RPN1001V) for one hour. After rinsing, sections were incubated with ABC kit for 30 minutes, and rinsed again with PBS. Sections were then reacted with DAB and H_2O_2 (kit from Abcam, used according to manufacturer's instructions) for five minutes. The reaction was stopped with distilled water. Sections were mounted from PBS onto gelatinized microscope slides, dehydrated through an ascending series of ethanol (70, 90 and 100 % for two minutes each) followed by two times two minutes in xylene, dried and coverslipped with Entellan.

Scanning and image pre-processing

Sections were scanned with a 20× objective using a Zeiss Axioscan Z1 scanner (Carl Zeiss MicroImaging, Jena, Germany) and loss less TIFF files exported from the Zen software (RRID:SCR_013672). The TIFF images were renamed to reflect their serial order, and sections that had been horizontally flipped during mounting were mirrored. Images were downscaled to the lowest resolution giving satisfactory segmentation of cell bodies with the ilastik software (15 % and 10 % of their original width for parvalbumin and calbindin images, respectively). Mirroring, renaming and resizing steps were performed using the Transform function of the Nutil software (v.0.4.01, RRID:SCR_017183; Groeneboom et al., 2020). Distortions and dislocation of individual tissue pieces introduced during processing and mounting were corrected using Adobe Photoshop. We moved and mirrored image parts to reconstruct normal section appearance. For parvalbumin sections, such corrections were applied to the original TIFF images. However, the calbindin TIFF images were too large to be opened in Adobe Photoshop or similar software, and correction of section parts were therefore only applied to the downscaled images.

DATA ANALYSIS

We used the QuickNII-ilastik-Nutil (QUINT) workflow to extract and quantify labelled cells from microscopic images of calbindin- and parvalbumin stained sections (Yates et al., 2019). Through this workflow, images are spatially registered to atlas using QuickNII; objects-of-interest (in our case, cells) are segmented from the images using ilastik; and the segmented objects are quantified using Nutil. To extrapolate estimates for total numbers and volumetric densities, we further post-processed the QUINT results. Lastly, we performed a comparative analysis of parvalbumin neurons in the rat and mouse hippocampal region. The detailed methods of each step of the QUINT workflow, the post-processing of the results, and the comparative analysis is described below.

Atlas registration

Serial section images were spatially registered to common 3-D brain reference atlases using the QuickNII software v2.2 (RRID:SCR_016854; Puchades et al., 2019), bundled with the Allen Mouse Common Coordinate Framework, version 3 of the template, 2017 edition of the delineations (Wang et al., 2020; here referred to as CCFv3-2017) and the Waxholm Space atlas of the Sprague-Dawley rat brain, version 1.01 of the template and version 2 of the delineations (Papp et al., 2014; Kjonigsen et al., 2015; here referred to as WHSv2). First, section images were registered using QuickNII to identify section positions and deviations from the standard planes. For coronally oriented sections, the anatomically distinct landmarks were the

genu of the corpus callosum, the crossing of the anterior commissure, and the rostral appearance of structures such as nucleus accumbens, caudoputamen, and dorsal hippocampus. The superior and inferior colliculus, as well as the inferior olive, provided important anatomical landmarks in more posteriorly located sections. For horizontally oriented sections, the registration was primarily based on the anterior commissure, the dorsal appearance of the hippocampus and caudoputamen, the olfactory bulb and the piriform cortex. A second researcher verified all registration results. The affine registration with QuickNII yielded custom atlas plates matching each section image. To further optimize registration, the custom atlas images were non-linearly transformed using the software tool VisuAlign v0.8 (RRID:SCR_017978). We first focused on fitting the template to the outer edges of the section, and secondly adjusted it to refine the fit of major landmarks situated deeper in the brain (e.g. striatum, globus pallidus, hippocampus). The high-resolution microscopic images with their custom atlas overlay images are organized and disseminated to an interactive web-microscopy viewer via the Navigator N3 data system at the University of Oslo. A forerunner of this system is described by Moene et al. (2007).

Image segmentation

Pixel classification with ilastik. Images were segmented using the pixel classification pipeline in ilastik (RRID:SCR_015246; v.1.3.3), which allows classification of features on a pixel level on a scale up to 10 by 10 pixels. We assigned two label classes termed “cell” and “background”. During segmentation, we placed labels throughout different regions and in all the training sections until the segmentation was deemed satisfactory. We trained one classifier per image series (i.e. one per animal). For each series, we used every fifth image for training and then applied the classifier to all images using the Batch Processing function in ilastik.

Removal of artefacts and incorrectly segmented objects. Overall, the classifiers produced by the pixel classification pipeline distinguished objects of interest from background with relatively high accuracy. Still, some artefacts and incorrectly segmented objects occurred. The ilastik software includes an object classification pipeline that allows for distinguishing artefacts, which is especially useful when these are very different from the objects of interest. However, in our material incorrectly segmented objects (e.g. neurites) resembled the objects of interest in size and shape. Therefore, we visually inspected all segmentation images to identify incorrectly segmented objects or artefacts, and removed these manually using NIH ImageJ. Most artefacts segmented as “cell” were seen around the edges of the sections and in relation to blood vessels and ventricles. Example images, segmentations and atlas overlays are shown in Supplemental Figure 4.

Quantification of segmented objects

We used Nutil Quantifier (v.0.4.02) to combine customized atlas maps from QuickNII (refined and exported using VisuAlign) with segmented images from ilastik. The pixel size cut-off function was used to exclude objects representing fragments or small artefacts; a cut-off of 4 pixels was chosen for both parvalbumin and calbindin datasets, based on visual inspection of segmented images.

The regions in the CCFv3-2017 are more fine-grained than the WHSv2. To achieve better correspondence with the granularity of the rat brain atlas, small regions and individual cellular layers in CCFv3-2017 were grouped into more coarse areas (e.g. primary motor cortex, CA1 of the hippocampus) using the “custom regions” feature of Nutil Quantifier. This reduction of granularity of atlas delineations was also motivated by the need to compensate for inaccuracies in the spatial registration of images to the common 3D atlas, which primarily impacts the precision of registration of small brain regions. Excel sheets indicating the organization of custom atlas regions are provided with the derived datasets and can be re-used in new analyses with Nutil Quantifier. Post-processing of numerical data (correction and extrapolation to whole regions and volumetric densities, described below) from mouse brains was performed on the numbers from these

aggregated custom regions. The numbers per individual region in the CCFv3-2017 were also extracted with Nutil Quantifier and included in the derived data files. The custom regions used in the present analyses are given in Figure 1.

Post-processing of Nutil Quantifier results

The output reports from Nutil contain the total number of segmented objects counted in every sampled section through each atlas region, given as counts per region, section, and region for the whole brain. These numbers represent all objects counted in all the images investigated. Additionally, damaged or missing parts of individual sections might influence results. To correct for the tissue sampling and missing tissue parts, we implemented a series of post-processing steps to extrapolate Nutil Quantifier numbers to reflect densities and total number estimates. First, we used the sectional reports to compile numbers per section for each region in a new spreadsheet. For all series, we manually inspected the quality and completeness of each section image. Whenever a part of the brain was damaged or missing in a section, or staining quality was deemed suboptimal, we identified which region(s) of the brain this affected. For every such instance, we replaced the Nutil Quantifier results according to the following rules. If a section showed damage or suboptimal staining on one side of the brain, we used the intact side as a reference and multiplied the number by two to get a bilateral estimate for the section. If a region was damaged or sub-optimally stained on both sides, we used an average of numbers obtained from the adjacent neighbouring sections. The adjusted section-by-section numbers were summed per region of interest in a second spreadsheet. On average, 20 % of the sections in a series needed some form of correction, typically meaning that numbers for one or a few regions were corrected as described above. Exclusion of whole sections from the analysis were very rarely necessary, and never for more than 4 % of all the sections within a series. Details on whether corrections were made (and if so, which ones) are provided as metadata with each of the datasets.

Secondly, to adjust for double-counting in volumetric extrapolation, we calculated an estimate of total numbers of cells in each region by using Abercrombie's formula (Abercrombie, 1946):

$$N = \frac{n \times T}{T + D}$$

Where N is the cell number, n is the number of counted profiles, T is the thickness of the sections, and D is the mean diameter of the profiles. The mean cell diameter was calculated by multiplying the average object area for all cells (generated by Nutil Quantifier) by the pixel scale of the images, and using this area (A) to calculate the diameter (D):

$$D = 2 \times \frac{A}{\pi}$$

The pixel scales for the section images used in ilastik were 8.6 pixels per μm^2 for rat and mouse parvalbumin section images, and 4.8 pixels per μm^2 for the mouse calbindin section images. The estimated diameter of the cells used in our calculations were 11.3 and 12.7 µm for mouse and rat parvalbumin neurons, respectively, and 7.9 µm for mouse calbindin neurons. Lastly, we multiplied the resulting number with the section sampling fraction (4 for parvalbumin datasets, 6 for calbindin datasets) to estimate the total number of cells per region.

To estimate volumetric densities, we divided the total number of cells for each region with the volumes of each atlas region, exported from the ITK-snap software using the "Volumes and statistics" function. The .xlsx files included in the derived datasets, published on EBRAINS.eu, contain all the raw and corrected numbers, as well as the region volumes used for calculations. The volumetric densities estimated here were compared against those reported by Kim et al. (2017) and others in the literature (see section on "Comparison of findings with data from previous reports" below).

Comparative analysis of parvalbumin neurons

To compare the total number and density of parvalbumin neurons in the mouse and rat hippocampal region, hippocampal data from regions in the CCFv3-2017 were grouped to correspond with rat brain regions defined in the WHSv2 rat brain atlas. Most areas of the hippocampal region were highly comparable between the atlases, in terms of nomenclature, anatomical position and shape of the regions (Figure 6). The regions of Ammon's horn and the dentate gyrus were highly similar. The prosubiculum of the CCFv3-2017, intercalated between the subiculum and the CA1, was grouped as part of the subiculum, while the postsubiculum was included in the presubiculum, as this term is commonly used to refer to the dorsal presubiculum (Taube, 2007; Taube et al., 1990). The perirhinal and ectorhinal cortices in the CCFv3-2017 was considered to correspond to WHSv2 perirhinal area 35 and 36, respectively. Lastly, the postrhinal cortex (POR), was present in both the CCF and WHSv2, but with a much narrower dorsoventral extent in the CCFv3-2017 than the WHSv2. In the WHSv2, the POR lines the caudal pole of the lateral and medial entorhinal cortex dorsally; in the CCFv3-2017, however, the POR does not extend to the most caudal part of the cortex. At this level, a cortical region termed the posterolateral visual area is included in the CCFv3-2017. Anatomically, the combined postrhinal and posterolateral visual area in the CCFv3-2017 resemble the POR in the WHSv2. We therefore included both of these in the postrhinal cortex for our comparative analysis. Figure 6 shows hippocampal regions in the two atlases and the mapping of CCFv3-2017 to WHSv2 regions.

Spatial distribution analysis. To explore and compare possible topographical distribution gradients of parvalbumin neurons in the mouse and rat parahippocampal region, we averaged the section-by-section density of parvalbumin neurons across animals and assessed whether densities of parvalbumin stained neurons changed along the dorsoventral axis of each subregion. To get numbers that could be compared for each level, we calculated volumetric densities per section as follows. First, we calculated corrected numbers of cells for each atlas region per section by applying Abercrombie's formula to the section-wise numbers. Then, for each atlas region, we multiplied the region area in pixels (extracted from Nutil Quantifier reports) by the pixel scale (see above). For each section, we then divided the corrected number of cells per region by the region area, and divided this by the section thickness (Keller et al., 2018) to get the volumetric density:

$$\mathrm{vN} = \frac{n}{T}$$

Where vN is the volumetric density, n is the corrected two-dimensional cell count, and T is the thickness of the section. This gave the density per μm^3; lastly, to get numbers per mm^3, we therefore multiplied these by 10^9.

We next sorted sections according to their dorsoventral level for each animal, and averaged the density of neurons per level across animals. Each subregion was then represented in a spreadsheet as a row containing the average parvalbumin neuron density for each dorsoventral level (one column per level). We applied conditional formatting to each row so each cell was colour-coded in a gradient according to its value, with the lowest number for each row coded light yellow and the highest number coded dark orange. These colour-coded rows were inspected for cases of clear dorsoventral gradients and copied to Adobe Illustrator to be shown in figures (see Results).

METHOD VALIDATION

Comparison of findings with previous reports

Kim and colleagues (2017) mapped parvalbumin interneurons across the whole mouse brain using transgenic mice and image segmentation based on convolutional neural networks. They shared all the total number and density estimates through their publication, which we downloaded and used for comparison. They used a custom-built three-dimensional version of the original (two-dimensional) Allen Reference Atlas of the mouse brain (Dong, 2008). The nomenclature used for this version is similar, but not identical, to the one in the version we used in our analysis (CCFv3-2017). We therefore mapped the results found in their files to the custom regions used in our analysis (see above). Kim et al. (2017) reported values for both male and female mice, and reported that several subcortical structures are sexually dimorphic. Given this finding, and the fact that our mouse parvalbumin data were obtained from males, we used only the results from their male subjects (n = 5) for comparison to our results (n = 4).

We also queried the literature to find estimates of the same cell types as those quantified here. To this end, we searched for 1) the RRIDs and catalogue numbers of the antibodies used in our study (using Google Scholar) and 2) articles that mentioned both stereology and “parvalbumin” or “calbindin” in the title or abstract (using PubMed). For each search, all results were screened manually and included if they presented relevant data (total number or density estimate of parvalbumin or calbindin cells in rats or mice).

The following searches were performed:

1. Google Scholar search for RRID:AB_2631173. Performed 14.04.2020; 31 results, 2 included.

2. Google Scholar search for RRID:AB_477329. Performed 20.04.2020; 81 results, none included.

3. Google Scholar search for RRID:AB_10000347. Performed 21.04.2020; 87 results, none included.

4. Google Scholar search for ((rat) OR (mouse)) AND (Swant PV27) AND (stereology OR stereological). Performed 14.04.2020; 18 results, 1 included.

5. Google Scholar search for ((rat) OR (mouse)) AND (PARV-19) AND (stereology OR stereological). Performed 20.04.2020; 61 results, 2 included.

6. Google Scholar search for ((rat) OR (mouse)) AND (“Swant 300”) AND (stereology OR stereological). Performed 21.04.2020; 21 results, none included.

7. PubMed (via Ovid Medline) search for: (rat or mouse or rodent).tw,kf AND stereolog*.tw,kf. AND parvalbumin.tw,kf. Performed 14.04.2020; 59 results, 14 included.

8. PubMed (via Ovid Medline) search for: (rat or mouse or rodent).tw,kf AND stereolog*.tw,kf. AND calbindin*.tw,kf. Performed 21.04.2020; 38 results, 3 included

We supplemented this search with references from a recent review of number estimates in the mouse brain (Keller et al., 2018) and from our previously published database of literature-derived quantitative estimates in the basal ganglia (Bjerke et al., 2019, 2020)

Validity of segmentations

The results obtained with the QUINT workflow were benchmarked against prior manual counts from both parvalbumin and calbindin stained material that were used as a guide during the segmentation process. Manual counting was performed on a subset of the material by annotating each labelled cell in Adobe Photoshop (RRID:SCR_014199). The annotated cells were subsequently quantified using Nutil, as described above. Manual counting was performed for each section throughout the calbindin stained anterior cingulate cortex (sections s103 – s175 from mouse 10), the parvalbumin stained entorhinal cortex (s019 – s044 from rat 25205), and for one whole hemisphere from each of the stains (s151 from mouse10 and s028 from rat 25205). The regions of interest were defined by the QuickNII atlas maps for the evaluated sections and were thus identical for the quantification of manual and ilastik segmentations.

Reliability of segmentations

We assessed both intra- and interrater reliability by segmenting material from one of the series (parvalbumin stained sections from rat 25205) several times. Intrarater reliability was assessed by one researcher segmenting the same material three times. The first and second segmentation was performed within the same week, while the last one was done six weeks later.

In a pilot study of interrater reliability, we considered the reliability of segmentations obtained by three researchers using the same material, but without clear guidelines for what to consider a labelled cell. We observed, both qualitatively and quantitatively, that results varied considerably between the three researchers. We therefore set out to do a more systematic assessment of interrater reliability, with clear instructions on how to perform the segmentation with ilastik. One researcher performed an initial segmentation and wrote instructions for its replication. The same materials and instructions were then presented to five other researchers for segmentation. The instructions gave a description of objects considered to be cells and example images of segmentation results. In addition, information was given on how to train the ilastik classifier, with instruction to not label pixels in oversaturated areas (specifically, the cerebellum and reticular nucleus of thalamus). Researchers were also given access to the segmentations overlaid on the original (high-resolution) images via an online viewer system, and were instructed to use these actively to verify similarity of segmentations. The full instructions as given to the researchers is included in the section below. Each researcher then ran their classifier on the full set of images from rat 25205. Objects in the resulting segmented images were quantified using Nutil quantifier, as described above.

Documentation for segmentation of parvalbumin cells in rat 25205

Instructions provided to researchers:

Goal. The goal of this exercise is to reproduce a segmentation (“target segmentation”) made by one researcher as faithfully as possible. The original segmentation was made with the aim of extracting parvalbumin positive cell bodies from DAB-stained images. The cells are generally easy to recognize, but there are variations across the material that makes some profiles more difficult to determine. In the more difficult cases, researchers might have different opinions on what should be considered a cell. I have aimed to provide the sufficient and necessary documentation with respect to what I have considered a cell when segmenting this material. It is important that you consider the provided examples and attempt to replicate this, regardless of whether you agree with the definitions and segmentations made here.

Training images. The training material includes very fifth section throughout the series, starting with s003 and ending with s053. Images are 15 % of original tiff resolution (with original tiffs being 50 % of original CZI file).

Cell criteria. A combined evaluation of the following criteria was used to decide whether an object is a cell or not:

- clearly distinguished from the background
- round, ovoid, triangular, or multipolar in shape
- medium, darkly, or intensely stained
- size substantial enough to support that the object is a cell and not axonal or dendritic fragments

See “Examples of manually annotated cells” below for examples.

Training in ilastik. Certain areas are so heavily labelled or contains so much stained neuropil that they should be excluded from the brain-wide analysis so as not to compromise the quality of the remaining classifier. For this reason, do not segment pixels in the cerebellum or reticular nucleus of the thalamus. Before starting, see the examples of manual annotations and target segmentations in the end of this document. High-resolution images with target segmentations overlaid are available via the Navigator3 system, and can be used as a reference during segmentation.

1) Select all features
2) Create two labels: cells and background
3) Use the thinnest brush stroke (1 px)
4) Label some clear examples of cells, and label directly adjacent pixels as background.

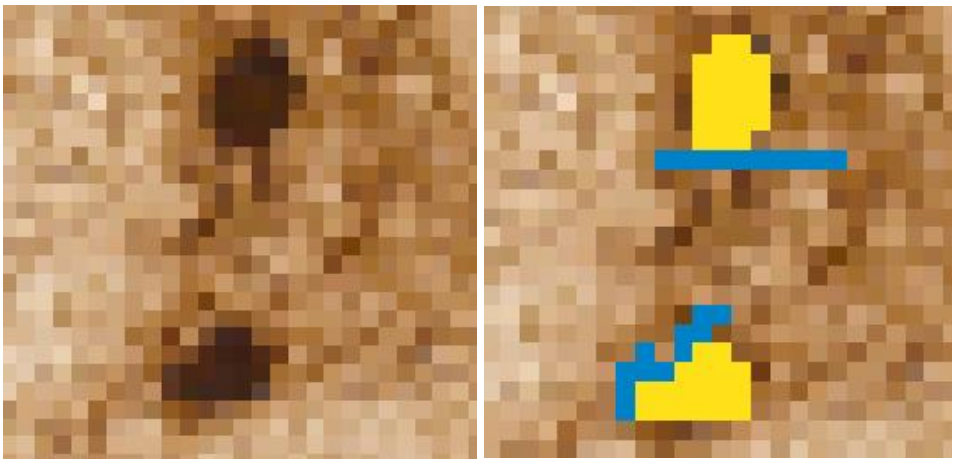

Step 2 illustration

5) Label some cells that are closely placed, and label the area between them as background
6) Place some background labels in appropriate areas, especially in regions with a lot of stained neuropil and around ventricles where staining is strong but not representing cells.

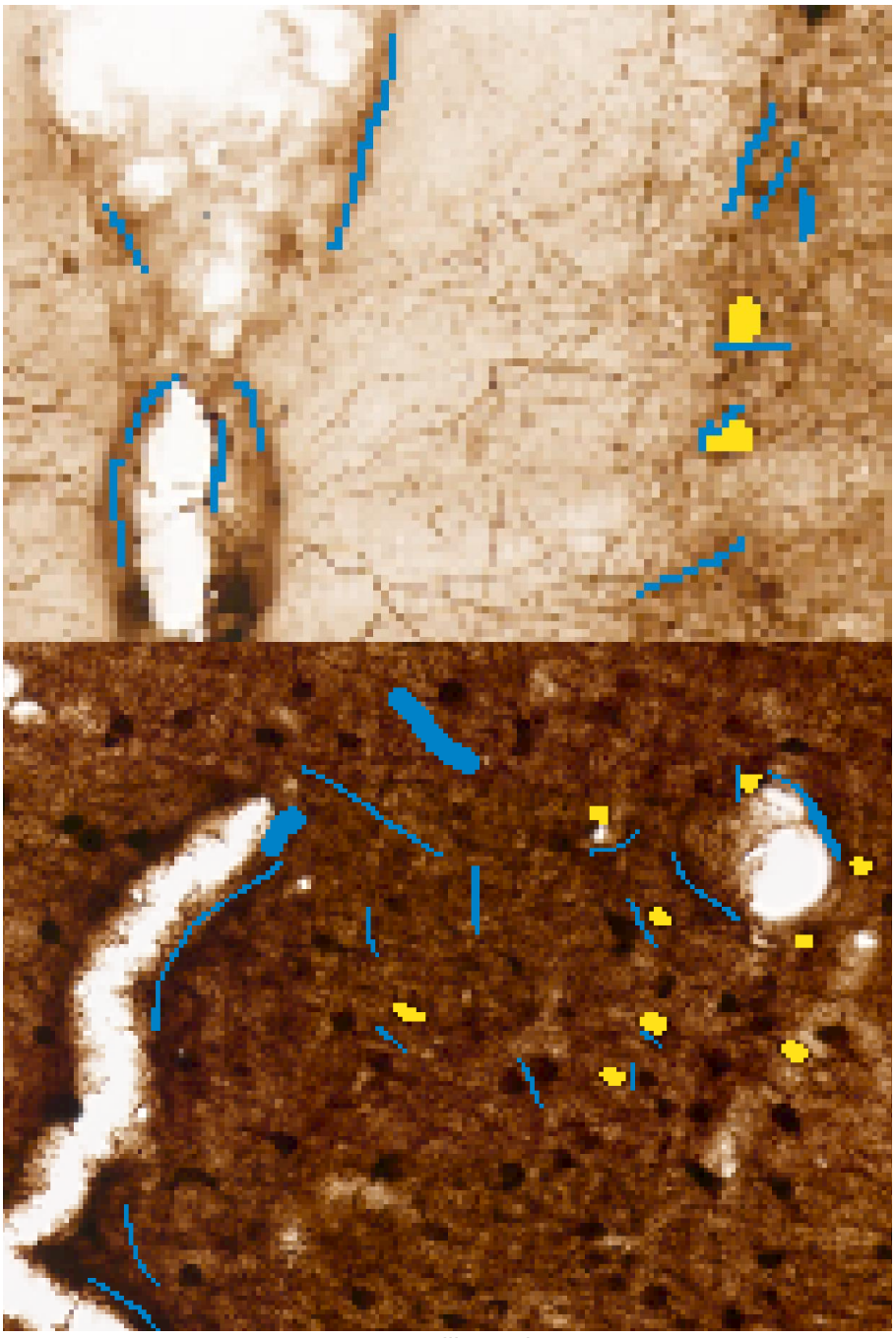

Step 3-4 illustration

7) Make sure to do steps 3-5 for areas of different intensities and across anatomical regions (cortex, hippocampus, striatum) and training sections. Use a bigger (5 or 7 px) brush to label more extensive areas of background.
8) Use live update and toggle the uncertainty filter to identify objects for which the classifier needs further input
9) Label cells for which the classifier is uncertain until the uncertainty is restricted to haloes surrounding cells, i.e. until there is little uncertainty in the center of the objects. Make sure to label areas of background at the same time.

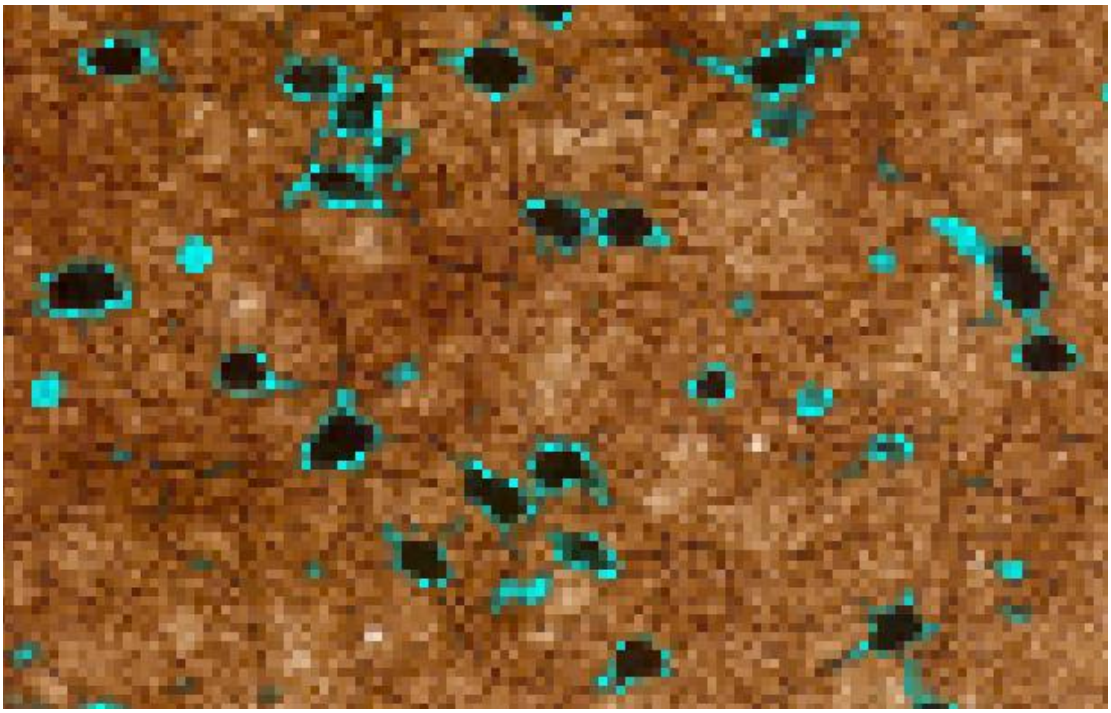

Uncertainty filter applied. Cells are recognized with confidence, despite uncertainty at their edges.

10) Repeat step 8 across all training images, and make sure to visit representative areas (including cortex, striatum, hippocampus, globus pallidus, basal forebrain, olfactory bulb).
11) See target segmentation images in Navigator to evaluate whether results are satisfactory. Go through all training images with reference to the segmented training images. If you have a lot of undesired pixels segmented as cells, label more background pixels. Note that a pixel size filter of 4 pixels will be applied to the segmentations, so fragments smaller than this will not affect the results.

Examples of manually annotated cells

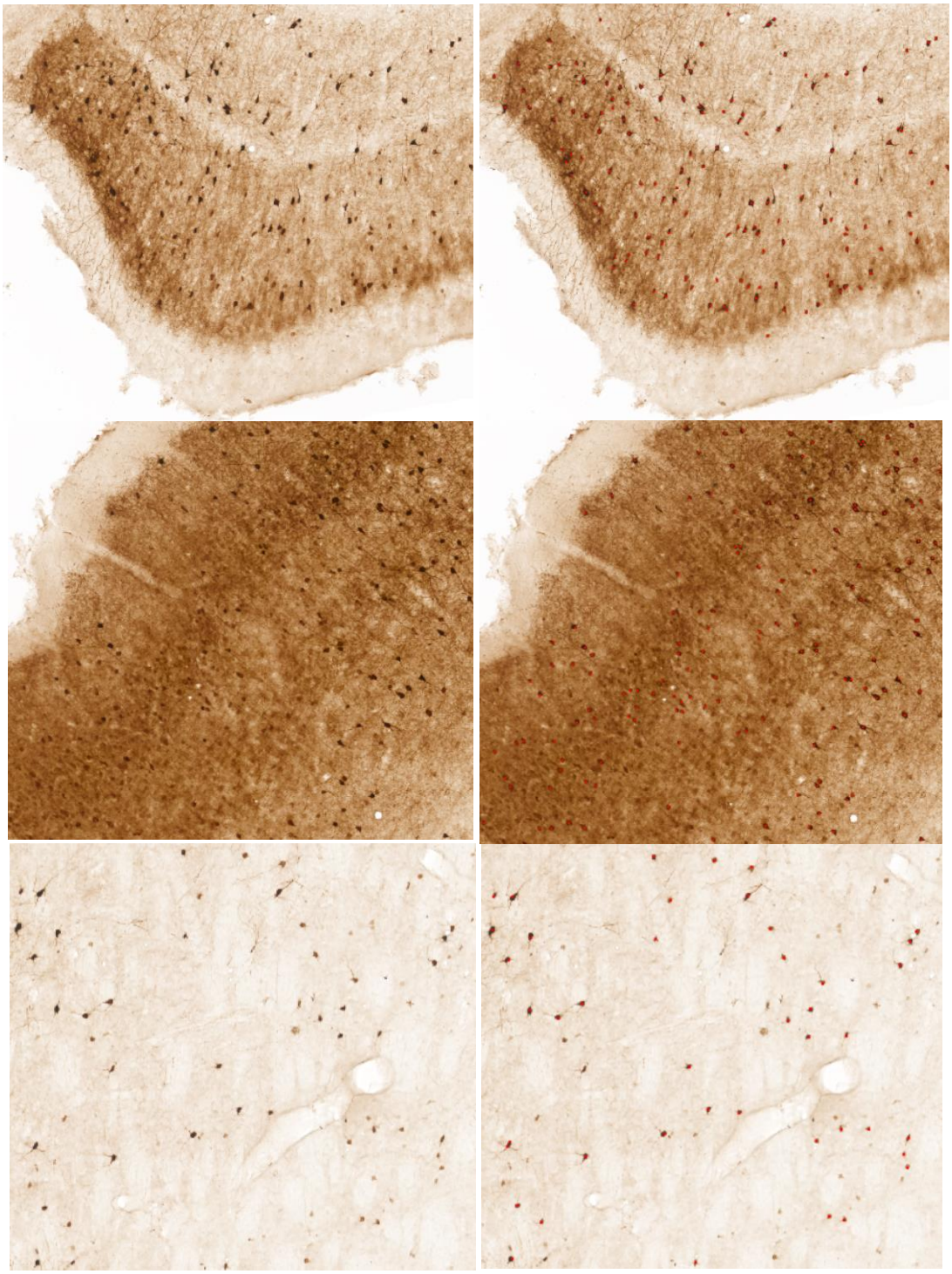

Examples images (left) and the same images with manually annotated cells. The examples are from medial entorhinal cortex (upper), neocortex (middle) and striatum (lower) from s028 of the training images. Very lightly stained objects, or objects that do not have a clear cell shaped outline easily distinguished from background staining, are here not considered to represent cell profiles.

Examples of target segmentation results

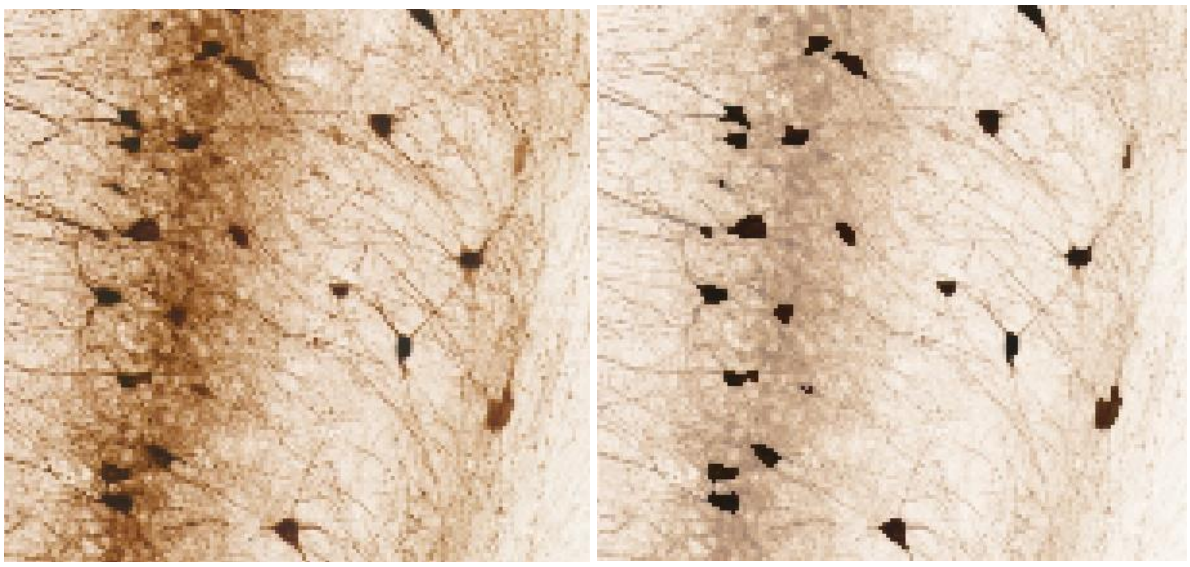

Hippocampus, s014

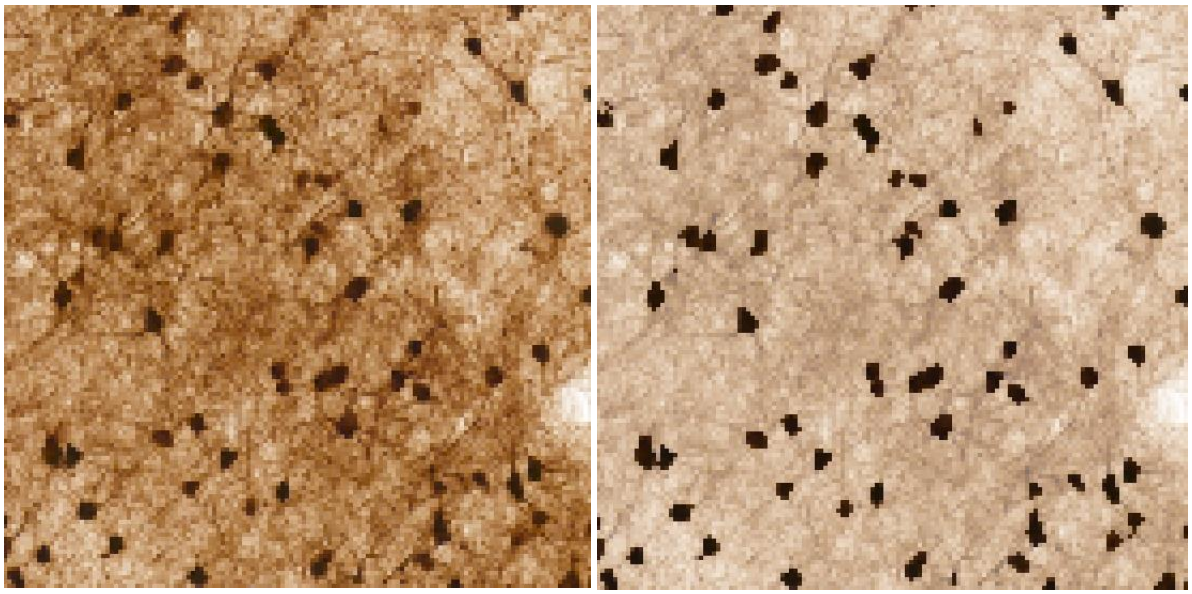

Cortex, s014

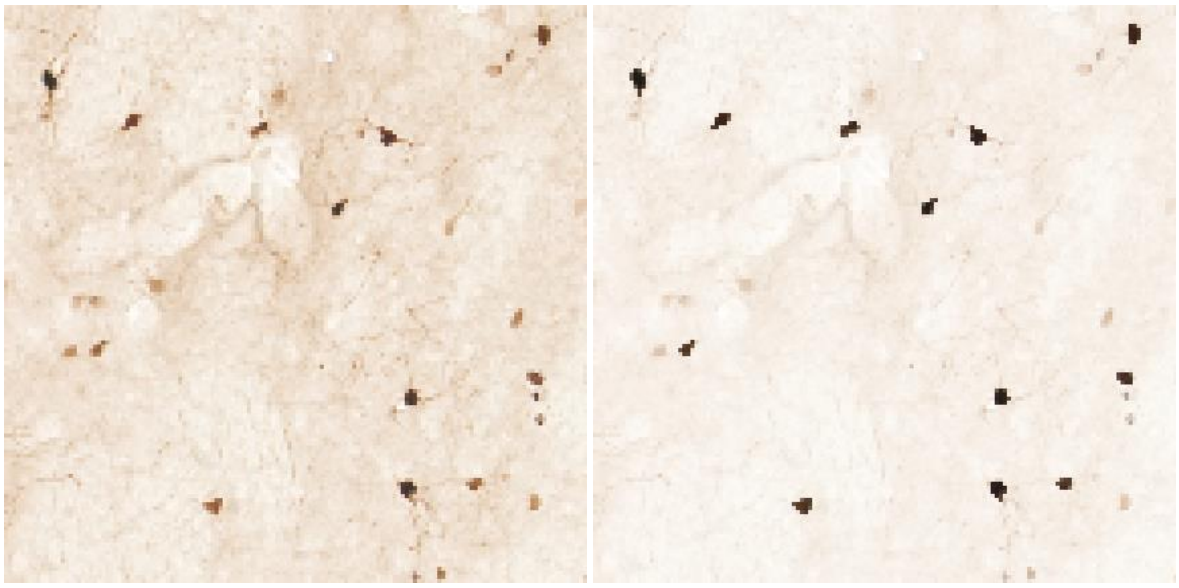

Caudoputamen, s025

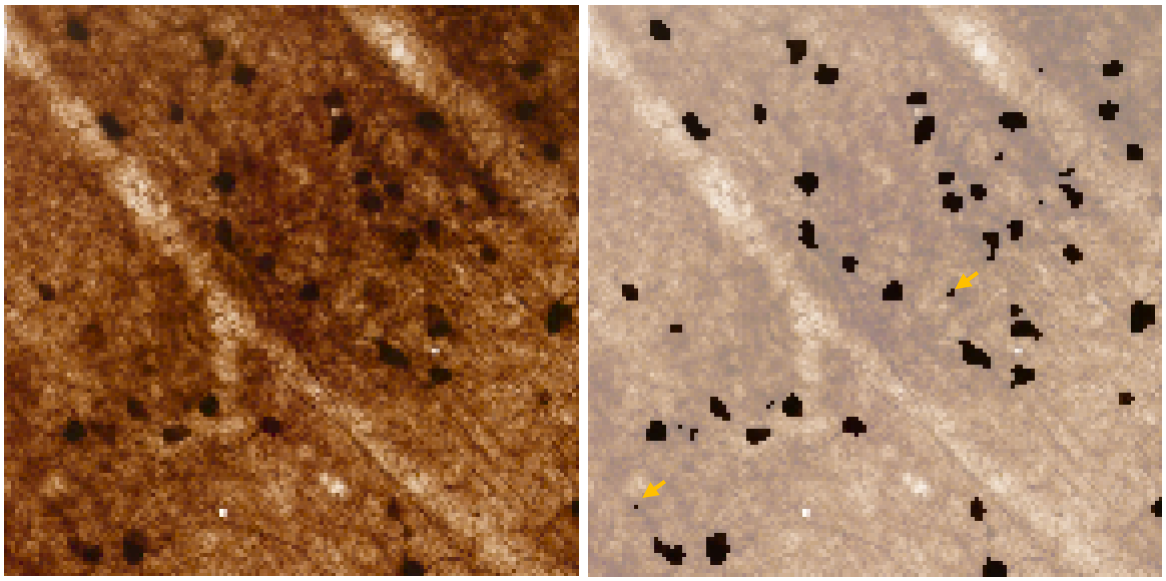

Cortex, s025. Yellow arrows point to examples of fragments that will be filtered out later based on size and thus will not affect count results.

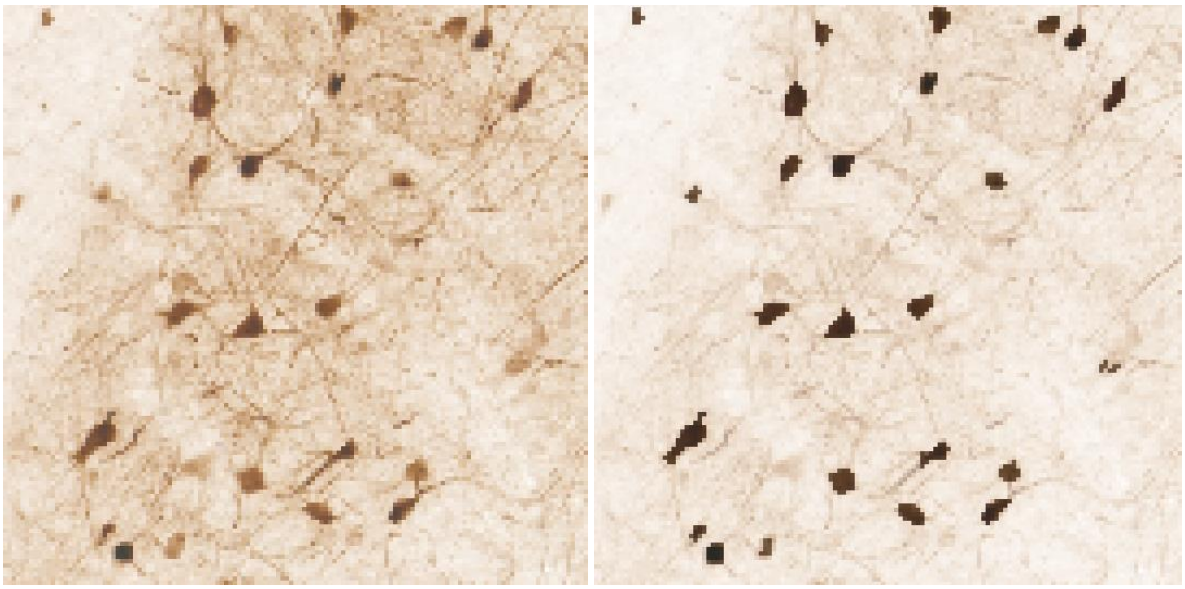

Globus pallidus, s038

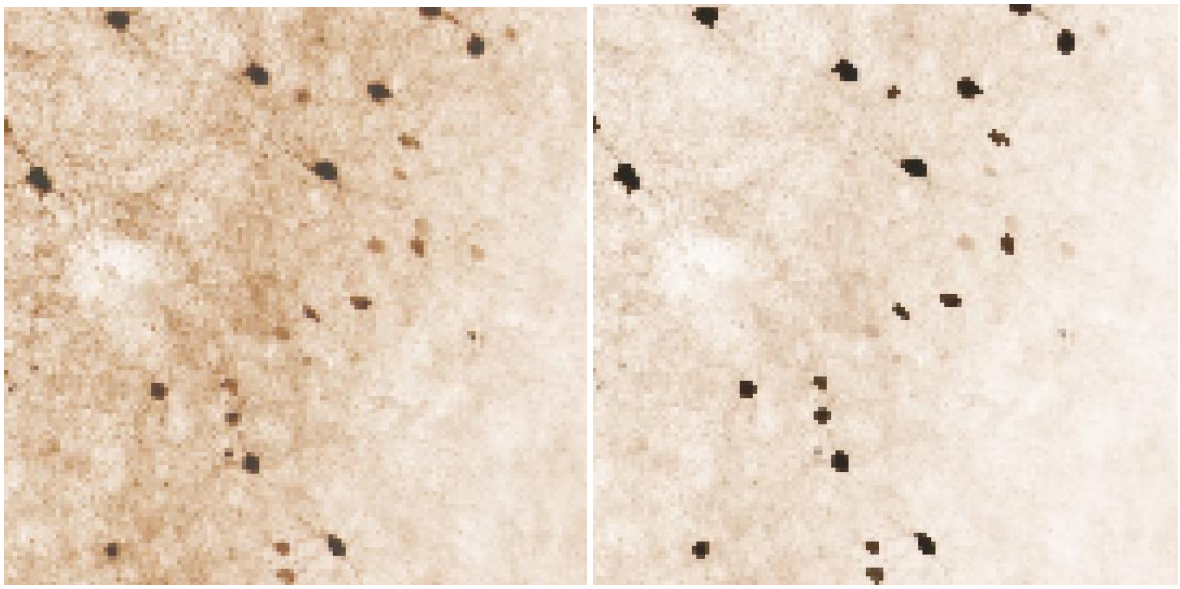

Cortex, s038

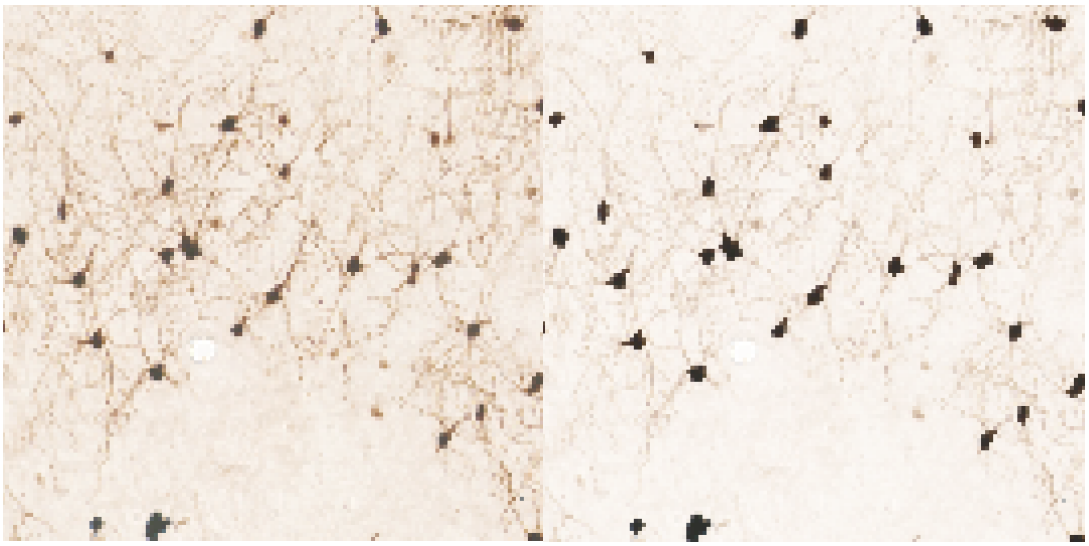

Olfactory bulb, s038

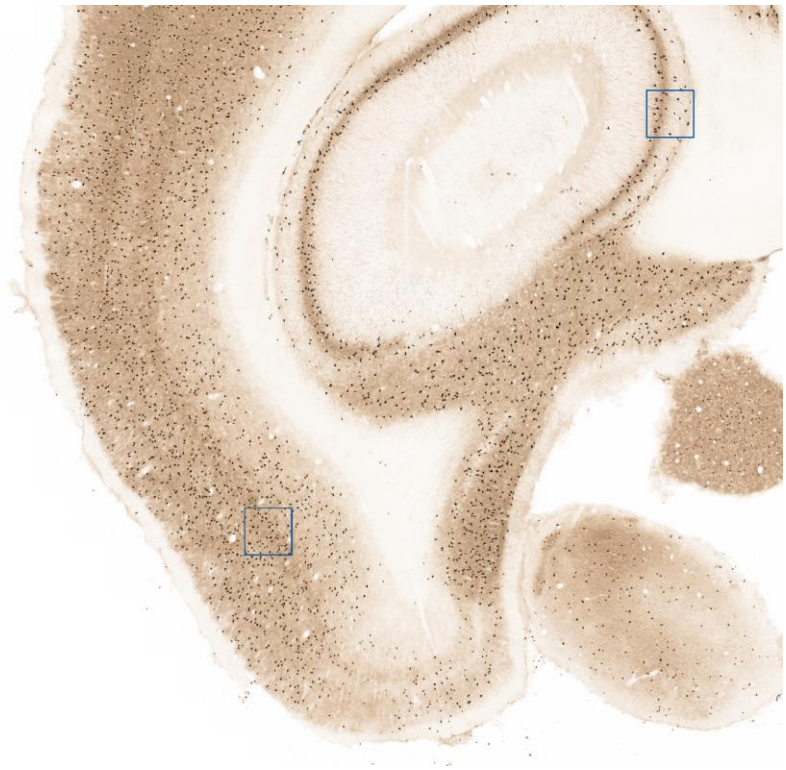

Hippocampus and cortex parts shown in examples above, s014

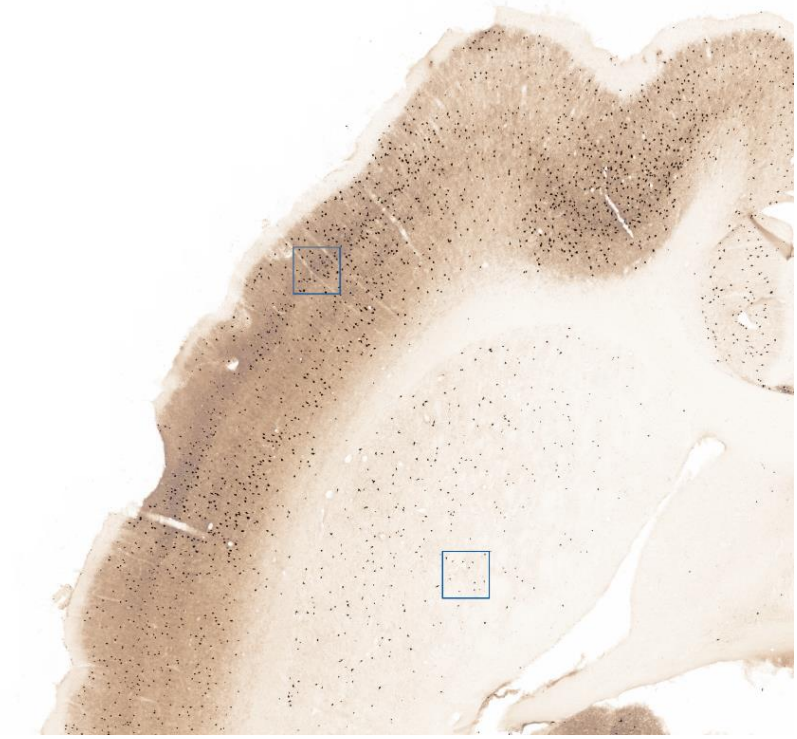

Caudoputamen and cortex parts shown in examples above, s025

Globus pallidus, cortex, and olfactory bulb parts shown in examples above, s038

QUANTIFICATION AND STATISTICAL ANALYSIS

Quantitative data throughout this paper are reported as mean ± SEM. Summary statistics were extracted using Microsoft Excel (RRID:SCR_016137). Exact values of n, representing the number of animals, are given in the result section.

Supplemental references

Aika, Y., Ren, J.Q., Kosaka, K., and Kosaka, T. (1994). Quantitative analysis of GABA-like-immunoreactive and parvalbumin-containing neurons in the CA1 region of the rat hippocampus using a stereological method, the disector. Exp. Brain Res. *99*, 267–276.

Barinka, F., Salaj, M., Rybář, J., Krajčovičová, E., Kubová, H., and Druga, R. (2012). Calretinin, parvalbumin and calbindin immunoreactive interneurons in perirhinal cortex and temporal area Te3V of the rat brain: Qualitative and quantitative analyses. Brain Res. *1436*, 68–80.

Bjerke, I., Puchades, M., Bjaalie, J., and Leergaard, T. (2019). Database of quantitative cellular and subcellular morphological properties from rat and mouse basal ganglia (Human Brain Project Neuroinformatics Platform).

Kaalund, S.S., Riise, J., Broberg, B. V., Fabricius, K., Karlsen, A.S., Secher, T., Plath, N., and Pakkenberg, B. (2013). Differential expression of parvalbumin in neonatal phencyclidine-treated rats and socially isolated rats. J. Neurochem. *124*, 548–557.

Kägi, U., Berchtold, M.W., and Heizmann, C.W. (1987) Ca^{2+}-binding parvalbumin in rat testis. Characterization, localization, and expression during development. J. Biol. Chem., *262*(15), 7314-7320.

Megahed, T., Hattiangady, B., Shuai, B., and Shetty, A.K. (2015). Parvalbumin and neuropeptide Y expressing hippocampal GABA-ergic inhibitory interneuron numbers decline in a model of Gulf War illness. Front. Cell. Neurosci. *8*, 1–12.

Moene, I.A., Subramaniam, S., Darin, D., Leergaard, T.B., and Bjaalie, J.G. (2007). Toward a workbench for rodent brain image data: Systems architecture and design. Neuroinformatics.

Pinol, M.R., Kägi, U., Heizmann, C.W., Vogel, B., Sequier, J.M., Haas, W., Hunziker. (1990) Poly- and monoclonal antibodies against recombinant rat brain calbindin D-28 K were produced to map its selective distribution in the central nervous system. J. Neurochem. *54*(6), 1827-1833.

Sanchez-Mejias, E., Nuñez-Diaz, C., Sanchez-Varo, R., Gomez-Arboledas, A., Garcia-Leon, J.A., Fernandez-Valenzuela, J.J., Mejias-Ortega, M., Trujillo-Estrada, L., Baglietto-Vargas, D., Moreno-Gonzalez, I., et al. (2020). Distinct disease-sensitive GABAergic neurons in the perirhinal cortex of Alzheimer's mice and patients. Brain Pathol. *30*, 345–363.

Shiraki, A., Tanaka, T., Watanabe, Y., Saito, F., Akahori, Y., Imatanaka, N., Yoshida, T., and Shibutani, M. (2016). Immunohistochemistry of aberrant neuronal development induced by 6-propyl-2-thiouracil in rats. Toxicol. Lett. *261*, 59–71.

Taube, J. (2007). The head direction signal: Origins and sensory-motor integration. Annu. Rev. Neurosci. *30*, 181–207.

Taube, J.S., Muller, R.U., and Ranck, J.B. (1990). Head-direction cells recorded from the postsubiculum in freely moving rats. II. Effects of environmental manipulations. J. Neurosci. *10*, 436–447.

Trujillo-Estrada, L., Dávila, J.C., Sánchez-Mejias, E., Sánchez-Varo, R., Gomez-Arboledas, A., Vizuete, M., Vitorica, J., and Gutiérrez, A. (2014). Early neuronal loss and axonal/presynaptic damage is associated with accelerated amyloid-β accumulation in AβPP/PS1 Alzheimer's disease mice subiculum. J. Alzheimer's Dis. *42*, 521–541.

Wang, C.Z., Yang, S.F., Xia, Y., and Johnson, K.M. (2008). Postnatal phencyclidine administration selectively reduces adult cortical parvalbumin-containing interneurons. Neuropsychopharmacology *33*, 2442–2455.